Nuclear Structure of Superheavy Elements

Rolf-Dietmar Herzberg

Abstract This chapter is dedicated to the nuclear structure of superheavy elements. It brings together all aspects of nuclear structure that have an influence on the stability of the nucleus on the one hand and that form the basis of experiments performed on superheavy elements to elucidate their nuclear structure on the other hand. The liquid drop model (LDM) is introduced and used to explain the limits of stability against fission, before the shell model is used to explain magic numbers and shell stabilization. Rotational properties of deformed nuclei are introduced and their sensitivity to the underlying nuclear structure is explored. The single particle structure and the influence of pairing on nuclei is discussed before experimental techniques for in-beam gamma and conversion electron spectroscopy are introduced. Finally spectroscopy following alpha decay is discussed.

1 Introduction

The atomic nucleus consisting of Z protons and N neutrons carries 99.9% of an atom's mass, yet it only occupies 10^{-15} of the atomic volume. With all the mass and charge compressed into such a small space it is easy to be tempted into treating the nucleus as a point charge with a positive charge $q = +Ze$ which determines the number of electrons (and thus the chemical element) and neglect its properties in first order when discussing atomic physics. However, if one looks closely the nucleus with its small but finite size has a profound impact on the atomic properties, and this impact is increasingly important the heavier and more highly charged the nucleus is. Details of the electronic structure of superheavy elements

R.-D. Herzberg (✉)
Department of Physics, University of Liverpool, Liverpool L69 7ZE, United Kingdom
e-mail: R.Herzberg@Liverpool.ac.uk

M. Schädel and D. Shaughnessy (eds.), *The Chemistry of Superheavy Elements*,
DOI: 10.1007/978-3-642-37466-1_2, © Springer-Verlag Berlin Heidelberg 2014

and consequences of relativistic effects from fast moving electrons are outlined by V. Pershina in "Theoretical Chemistry of the Heaviest Elements".

The largest breakthrough in our understanding of the shell structure of the nucleus came with the successful explanation of the nuclear magic numbers $Z = 2, 8, 20, 28, 50$ and 82 for protons and $N = 2, 8, 20, 28, 50, 82$ and 126 for neutrons in terms of a large and attractive spin-orbit interaction by Goeppert-Mayer and Jensen in 1948 [1, 2]. This led to the first predictions for superheavy shell closures in 1966 by Heiner Meldner [3] who calculated that $Z = 114$ should be the next closed proton configuration. More details of this development from first empirical postulates to detailed theoretical calculations are discussed by G. Herrmann in "Historical Reminiscences: The Pioneering Years of Superheavy Element Research".

This enhanced stability for certain "magic" configurations is analogous to the closed electron shells in noble gases. However, the nucleus can form such closed shell configurations for protons as well as for neutrons, leading to extra stability for doubly magic systems. The heaviest stable nucleus is the doubly magic ^{208}Pb, no other isotopes with $Z > 82$ are stable. However, several primordial isotopes with half-lives comparable to the age of the earth exist: ^{209}Bi ($T_{1/2} = 1.9 \pm 0.2 \times 10^{20}$ year) [4], ^{232}Th ($T_{1/2} = 1.4 \times 10^{10}$ year) [5], ^{235}U ($T_{1/2} = 7.04 \times 10^{8}$ year) [6], and ^{238}U ($T_{1/2} = 4.5 \times 10^{9}$ year) [7]. This exceptional stability can directly be traced to the underlying shell structure. The quest for superheavy elements is therefore identical with the quest for the next closed proton shell and the ultimate limit of stability of matter.

In Sect. 2 we will first look to the liquid drop model (LDM) to understand the limits of nuclear stability. The LDM is used to understand the fission process before we turn to the shell model to discuss the origin and nature of magic shell closures. We use these insights to define superheavy nuclei as those who owe their existence solely to the stabilizing effects of the underlying shell structure. Section 3 looks at rotational properties of deformed nuclei and explores ways in which the observed bands can help to determine the underlying nuclear structure. Section 4 finally turns to the underlying single particle structure and discusses pairing, nuclear g-factors and isomerism. The experimental methods used for nuclear structure studies of superheavy nuclei are explored in Sect. 5.

This chapter is not meant to replace a textbook on nuclear physics. It rather assumes a passing familiarity with nuclear physics and strives to point out those elements and properties, which have a direct bearing on structural studies of superheavy elements. This requires us to make many choices throughout the chapter, hopefully striking a balance between an introduction into the subject that will whet the readers appetite for further study and a reference for those interested in the broad picture only. For a small selection of recommended undergraduate texts on nuclear physics see, e.g., [8–10].

2 Bulk Properties of the Nucleus

2.1 The Liquid Drop Model

The binding energy of a nucleus consisting of Z protons and $N = A - Z$ neutrons is, to first order, well described by the LDM. The model was first proposed by Weizsäcker [11] and Bethe [12] and describes the nucleus as a charged droplet of nuclear incompressible "liquid" of constant density with the strong nuclear force holding the drop together and the Coulomb interaction pushing it apart. The nuclear volume is then directly proportional to the number of constituent nucleons and the nuclear radius is found to be $R(A) = r_0 \times A^{1/3}$ with the constant usually chosen as $r_0 = 1.2$ fm. We can write the mass equivalent energy of the nucleus in the form shown in Eq. 1. Note that in the literature authors often do not give the mass but the binding energy, which results in the opposite sign of all but the first two terms.

$$M(Z,A) = Zm_pc^2 + (A-Z)m_nc^2 - a_VA + a_SA^{2/3} + a_C\frac{Z(Z-1)}{A^{1/3}} + a_A\frac{(A-2Z)^2}{A} - a_P \tag{1}$$

with

$$a_P = \begin{cases} +\delta A^{-1/2} & N,Z \text{ both even} \\ 0 & \\ -\delta A^{-1/2} & N,Z \text{ both odd} \end{cases} \tag{2}$$

The bulk of the mass is made up by the masses of the protons and neutrons. The remaining terms describe the binding energy in a finite nucleus:

- a_VA: The *volume term* accounts for the binding energy of all nucleons as if they were surrounded by infinite nuclear matter. It does not depend on Z since the strong nuclear force acts on neutrons and protons alike. It is proportional to the volume of the nucleus.
- $a_SA^{2/3}$: The *surface term* corrects the binding energy for those nucleons close to the nuclear surface which do not feel an attractive nuclear force on all sides. It is analogous to a surface tension and proportional to the nuclear surface area.
- $a_CZ(Z-1)/A^{1/3}$: The *Coulomb term* accounts for the Coulomb repulsion between the Z protons in the nucleus. For heavy nuclei it is usually approximated as $a_CZ^2/A^{1/3}$.
- $a_A(A-2Z)^2/A = a_A(N-Z)^2/A$: The *asymmetry term* accounts for the difference between protons and neutrons and the Pauli principle.
- $a_P = \pm\delta A^{-1/2}$: The *pairing term* accounts for the tendency of nucleons to form pairs, which are more strongly bound than unpaired nucleons.

To understand the limits of nuclear stability it is clearly the binding energy that is crucial. Thus we examine the binding energy per nucleon $BE(A,Z) = (Zm_pc^2 + (A-Z)m_nc^2 - M(Z,A))/A$ as written in Eq. 3:

$$BE(A,Z) = a_V - a_S A^{-1/3} - a_C \frac{Z(Z-1)}{A^{4/3}} - a_A \frac{(Z-N)^2}{A^2} + \begin{cases} +\delta A^{-3/2} & N,Z \text{ even} \\ 0 & \\ -\delta A^{-3/2} & N,Z \text{ odd} \end{cases} \tag{3}$$

with the parameters a_V, a_S, a_C, a_A, and δ determined from fits to the entire Chart of Nuclei. A common parametrization is $a_V = 15.85$ MeV, $a_S = 18.34$ MeV, $a_C = 0.71$ MeV, $a_A = 23.21$ MeV, $\delta = 12$ MeV [13] . On average the binding energy per nucleon for nuclei around the valley of stability is found to be around 8 MeV. This simple picture will need to be modified significantly to take into account the effect of deformation and the underlying quantum shell structure of the nucleus.

In Fig. 1 we overlay the liquid drop binding energy per nucleon with the known limits of the chart of nuclei. Apart from very light nuclei, we find that nearly all nuclei lie within the contour for a binding energy per nucleon of 7.5 MeV. The notable exception comes at the upper end of the chart where the nuclei beyond Fm ($Z = 100$) all have lower binding energies. The stability of a nucleus against fission in this simple LDM can be parametrized by the fissility parameter

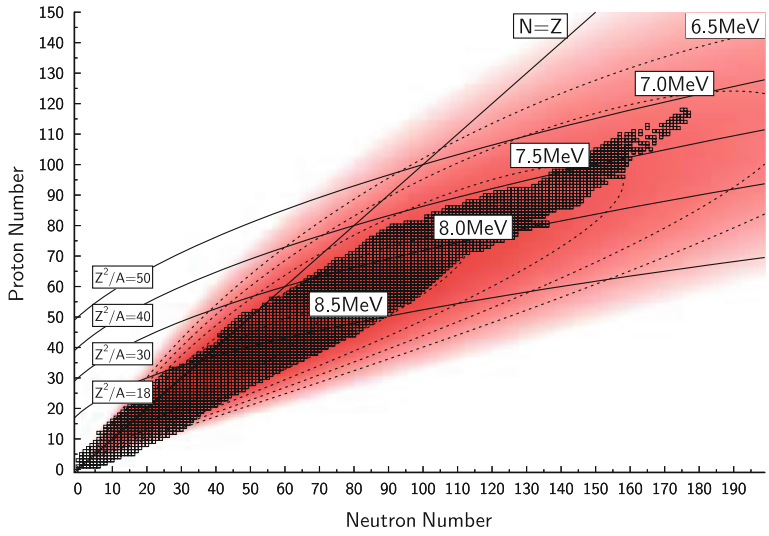

Fig. 1 Binding energy per nucleon in the liquid drop model. Isocontours for binding energies of 8.5, 8, 7.5, 7, and 6.5 MeV are shown, together with the line $N = Z$ and fissility contours $x = Z^2/A = 18, 30, 40, 50$. A fissility $x \simeq 40$ gives the limit of stability in the LDM. Nuclei beyond this line are stabilised entirely by shell effects

$x = Z^2/A$, which will be discussed in detail in Sect. 2.2. We therefore also overlay lines of constant fissility and find that these nuclei also have a high fissility. Indeed, it is in this mass region that the first spontaneously fissioning nuclei are observed.

The curved form of the line of stability with an increasingly strong deviation from the line $N = Z$ towards more neutron-rich nuclei can easily be understood from the LDM. Taking the derivative of $M(Z, A)$ with respect to Z while keeping A constant one obtains the relation for the maximum binding energy obtained for a given mass A at the proton number (Eq. 4)

$$Z \simeq \frac{4a_A + (m_n - m_p)c^2}{2\left(\frac{a_C}{A^{1/3}} + \frac{4a_A}{A}\right)} \simeq \frac{A}{2}\left(\frac{1}{1 + \frac{a_C}{4a_A}A^{2/3}}\right). \tag{4}$$

This form clearly shows the gentle curve of the line of stability towards the neutron-rich side. It is also the bane of experimental studies of superheavy elements, as one has to try to create a nucleus with a very high ratio of neutrons to protons N/Z from a reaction of lighter partners, which will have (much) smaller ratios of N/Z. Thus currently the study of superheavy elements is restricted to neutron deficient isotopes. In future radioactive beam facilities one can hope to use exotic beams with much higher N/Z ratios to create more neutron rich superheavy elements.

2.2 Spontaneous Fission

It is instructive to look in some detail at the fission process. We shall first treat the nucleus in the LDM discussed above. As the fission process leads to the release of a large amount of energy leaving the fission fragments in highly excited states, it is obvious that in first order only the three leading terms (volume, surface, and Coulomb) play an important role in the fission process. Note, however, that the underlying shell structure has a large influence on the detailed fission process and the distribution of the fragments in symmetric and asymmetric fission. As only a few nucleons get emitted in addition to the main fragments the ratio N/A for the fragments resembles that of the fissioning nucleus.

We are neglecting the effects of pairing as they are most important in the vicinity of the ground state and therefore play only a minor role in the fission process during which the nucleus becomes highly excited. Then Eq. 5 gives the binding energy of the nucleus in the LDM.

$$BE = a_V A - a_S A^{2/3} - a_C \frac{Z(Z-1)}{A^{1/3}} \tag{5}$$

We can model the onset of the fission process by evaluating the evolution of these three terms during a smooth transition from the spherical equilibrium shape with radius R to an ellipsoidal shape with long and short axes $a = R(1 + \delta)$ and

$b = c = R/(1+\delta)^{1/2}$. The volume term clearly stays constant with deformation. The surface area to first approximation increases to $S(\delta) = S_0(1 + 2\delta^2/5)$. Similarly the average distance between two protons increases and the Coulomb energy decreases to first order by a factor $E_C(\delta) = E_{C0}(1 - \delta^2/5)$. Equation 6 gives the binding energy as a function of deformation.

$$BE(\delta) = a_V A - a_S A^{2/3}\left(1 + \frac{2}{5}\delta^2\right) - a_C \frac{Z(Z-1)}{A^{1/3}}\left(1 - \frac{1}{5}\delta^2\right) \tag{6}$$

The energy gain then takes the form of Eq. 7.

$$\Delta E(\delta) = BE(\delta) - BE(0) = \frac{\delta^2}{5}\left[a_C \frac{Z(Z-1)}{A^{1/3}} - 2a_S A^{2/3}\right] \simeq \frac{\delta^2 A^{2/3}}{5}(a_C x - 2a_S). \tag{7}$$

The last form approximates $Z(Z-1)$ as Z^2 and writes the term in brackets in terms of the fissility $x = Z^2/A$. Thus Eq. 7 demonstrates the stability of the spherical equilibrium when deformations are small as well as the energetically increasingly favourable conditions for spontaneous fission with increasing fissility. Once deformation grows the first order discussion is no longer valid and higher order terms lead to the formation of a neck, and, finally, separation of the fragments. Other parametrizations for the fission process exist in the literature, see, e.g., [14]. Figure 2 shows the shape and height of the fission barrier for symmetric fission of a spherical nucleus with mass A and charge Z into two spherical fragments with $A/2$ and $Z/2$ and indicates the corresponding nuclear shapes. The height of the fission barrier can be approximated as shown in Eq. 8.

$$\begin{aligned} E_{fiss} \simeq & BE(A,Z) - 2BE(A/2, Z/2) + \Delta E(\delta) \\ = & a_S A^{2/3}\left(1 - 2\left(\tfrac{1}{2}\right)^{2/3}\right) + a_C \frac{Z^2}{A^{1/3}}\left(1 - 2\left(\tfrac{1}{2}\right)^{5/3}\right) + \frac{\delta^2 A^{2/3}}{5}\left[2a_S - a_C \frac{Z^2}{A}\right] \\ = & A^{2/3}\left(0.37 a_C \frac{Z^2}{A} - 0.26 a_S A^{2/3} + \frac{\delta^2}{5}\left[2a_S - a_C \frac{Z^2}{A}\right]\right) \end{aligned} \tag{8}$$

This leads to an energy gain for fissilities $x = \frac{Z^2}{A} \geq \frac{0.26 a_S}{0.37 a_C} \approx 18$.

We can also see that the liquid drop fission barrier vanishes completely for fissilities $x \geq 2a_S/a_C \approx 50$. The contours of constant $x = 18, 30, 40, 50$ are overlaid on Fig. 1 to show the influence of fissility on the limits of nuclear existence. The first spontaneously fissioning nuclei occur around $x \approx 40$, e.g., for ^{256}Rf. This is the limit of stability against spontaneous fission in the LDM. Any nuclei beyond this limit should not be stable against spontaneous fission and decay very quickly with half-lives shorter than 10^{-14} s. Experimentally a large number of nuclei beyond that point exist and decay predominantly though alpha or beta decay with half-lives of up to several seconds.

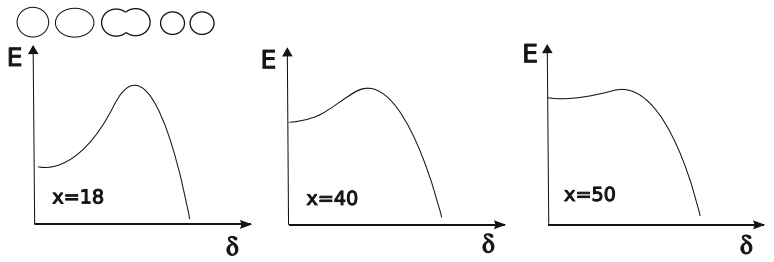

Fig. 2 Schematic illustration of fission barriers as a function of deformation parameter δ for several values of the fissility parameter x. The corresponding nuclear shapes are also indicated

Note that in the literature the fissility is often taken as the ratio of Z^2/A to a critical value $(Z^2/A)_{crit}$, which takes into account the proton-neutron asymmetry as defined in Eq. 9 [15] and is denoted by the capital letter X.

$$X = \frac{(Z^2/A)}{50.88[1 - 1.78((N-Z)/(N+Z))]} \tag{9}$$

This fissility X is a slowly varying quantity which, in the region above uranium, takes on values between 40 and 50.

We illustrate this behaviour in Fig. 3, where the experimentally obtained spontaneous fission half-lives are plotted against X for a number of heavy nuclei and compared to the fission half-life predicted by the LDM alone. The LDM half-

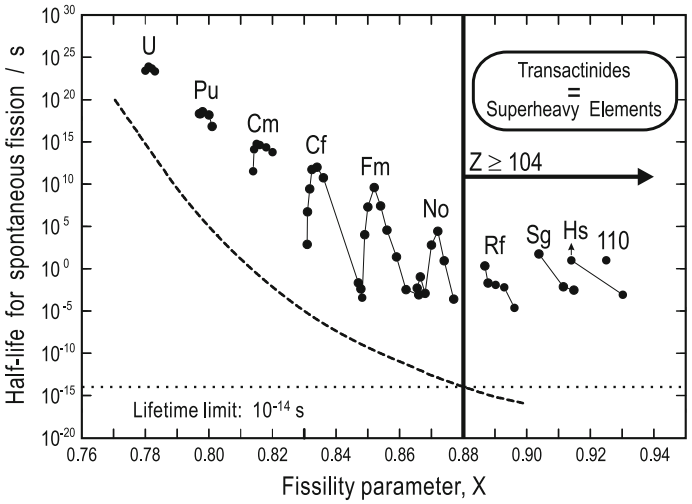

Fig. 3 Experimental spontaneous fission half-lives for even-even nuclei (*circles*) compared to the prediction of the liquid drop model as a function of the fissility parameter $x = Z^2/A$ (*dashed line*). The horizontal *dotted line* shows the minimum lifetime for the formation of a chemical element. Figure reproduced from [19] with permission

life dips below 10^{-14} s around $Z = 104$, as expected. This time is the minimum time required for a hydrogen molecule to form and gives an order of magnitude for the minimum time required for chemical processes.

We use this as a convenient working definition for superheavy nuclei: The superheavy nuclei are those that owe their stability solely to the underlying shell effects. See also the discussion by K. Moody in "Synthesis of Superheavy Elements" and G. Herrmann in "Historical Reminiscences: The Pioneering Years of Superheavy Element Research".

In reality the fission process is a lot more complicated than this simple picture implies. The nucleus has many degrees of freedom for its shape, and the fission barrier is the lowest barrier found in a large deformation parameter space, leading to symmetric and asymmetric fission, as dictated by the intricate interplay of all nucleons in an increasingly deformed potential. However, the simple arguments presented here serve to illustrate the principal limits to nuclear stability. For good starting points for further reading see, e.g., [14, 16–18].

2.3 The Spherical Shell Model

In order to obtain a more realistic understanding of the nucleus as a system of interacting protons and neutrons, we have to look at the underlying shell structure. While the LDM described in the previous section accounts for the bulk of the nuclear binding energy, it is insufficient to explain the experimentally observed deviations from a smooth behaviour observed for certain nucleon configurations. These nuclear "magic numbers" are $N, Z = 2, 8, 20, 28, 50, 82$ and $N = 126$. Experimental evidence for such underlying shell structure comes from several sources:

- Two nucleon separation energies. The binding energy associated with the removal of the last pair of protons or neutrons is very high at magic numbers, whereas it is very low for nuclei with two particles outside a magic shell.
- The probability to observe alpha decay is enhanced at proton and neutron numbers two higher than the magic numbers. This is most obvious in the neutron deficient $N = 84$ isotones where alpha decay first becomes a major decay mode in the nuclear chart. Alpha decays have also been observed for very neutron deficient Te isotopes in the vicinity of ^{100}Sn and they dominate in the heavy mass region beyond Pb. In the heavy mass region one can also observe that the alpha decays have relatively large Q-values above the shell while those for nuclei on the shell are significantly lower. For example the alpha decay of $^{216}_{88}\mathrm{Ra}_{128}$ has an alpha energy of $E_\alpha = 9.349$ MeV whereas the alpha decay of the neutron magic daughter $^{212}_{86}\mathrm{Rn}_{126}$ has an alpha decay energy of only $E_\alpha = 6.264$ MeV.
- Spherical shapes are predominantly found for nuclei with N or Z close to the magic numbers. In these nuclei the first excited state is typically at a very high excitation energy compared to neighbouring nuclei.

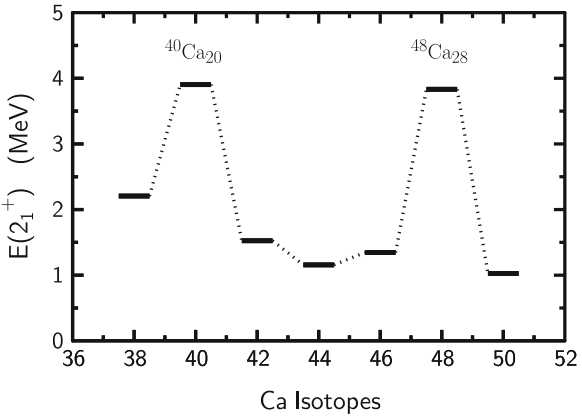

Fig. 4 Energy of the first excited 2^+ state in even nuclei in the calcium chain of isotopes. This chain contains two doubly magic systems with ^{40}Ca and ^{48}Ca. In both cases the first 2^+ state lies at a very high excitation energy compared to the neighboring isotopes

- The energy of the first excited 2^+ state has a local maximum. This experimental finding is illustrated in the calcium isotopes in Fig. 4.

The effect of nuclear shell closures is even more pronounced when both protons and neutrons have magic configurations, resulting in a significant increase in the nuclear binding energy. These doubly magic nuclei close to the line of stability are ^{4}He, ^{16}O, ^{40}Ca, ^{48}Ca, ^{56}Ni, ^{132}Sn, and ^{208}Pb. The more exotic doubly magic ^{48}Ni [20] and ^{100}Sn [21] lie at the extreme neutron deficient edge of the nuclear chart.

The nuclear shell model in its simplest form is based on several assumptions:

- The force between nuclei is attractive and has a short range. The short range is most easily seen by the near-constant nuclear density in the nuclear interior indicating that the attraction is dominant for directly neighboring nucleons.
- At short range the nucleons repel. This is a direct consequence of the Pauli exclusion principle and is usually referred to as the "hard core" of the nuclear interaction.
- Protons and neutrons move in the potential created by all other nucleons around them. Thus the nuclear potential itself is changed through the addition of nucleons. This is distinctly different to the atomic shell where electrons move in the Coulomb potential created by the pointlike nucleus which remains unchanged even if electrons are added to the atom.
- Nucleons move independently of each other and interact rarely. This seems counterintuitive at first. The nucleus is a dense object in which nucleons should "run into each other" all the time. However, nucleons are fermions and the Pauli exclusion principle means that they can only scatter into unoccupied levels. Thus two nucleons deep in the nuclear potential usually do not have sufficient energy to reach unoccupied levels and will not scatter unless they are near the Fermi level where unoccupied levels are more readily available.

Solving the resulting many body problem with a simple harmonic oscillator potential leads to wave functions which can be separated into a radial part $R(r)$ and an angular part characterized by the spherical harmonic functions $Y_{l,m}(\phi, \vartheta)$:

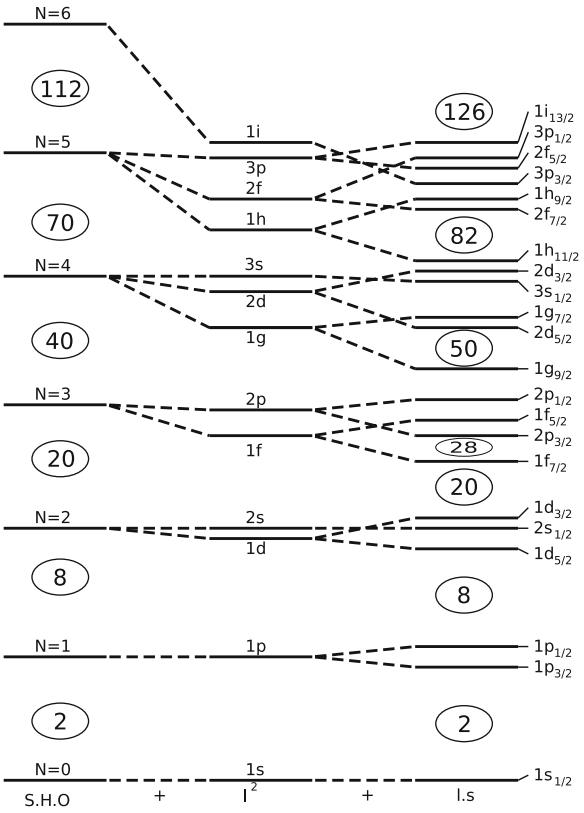

Fig. 5 Schematic representation of the states in the nuclear shell model. The oscillator shells on the *left* are first split into the individual subshells by deviations of the nuclear potential from the harmonic oscillator, before the spin-orbit interaction creates the groupings of states that produce the correct magic numbers above $N = Z = 20$. The diagram is schematic and not to scale

$$\psi(r, \phi\vartheta) = R(r)Y_{l,m}(\phi, \vartheta) \ . \tag{10}$$

We can now characterize the wave functions in that potential through four main quantum numbers, N, l, j, m. The oscillator quantum number N counts the number of oscillator quanta present and takes integer values $0, 1, 2, 3, 4, \ldots$. The orbital angular momentum l takes on integer values $l = N, N-2, N-4, \ldots, 0$ or 1 for states in each shell. The nucleons carry spin $s = 1/2$ which can be coupled to the orbital angular momentum to form the total angular momentum $j = l \pm 1/2$. Finally the projection of the total angular momentum j onto the quantisation axis is given by $m = -j, -j+1, -j+2, \ldots, +j-1, +j$. States are labelled by abbreviating l in the usual spectroscopic notation $s, p, d, f, g, h, i, j, \ldots$ for $l = 0, 1, 2, 3, \ldots$ and listed in the form l_j, such as $d_{5/2}$ and $i_{11/2}$. In case of ambiguities, the states can be distinguished by counting, i.e. we have the $1s_{1/2}$ state stemming from the $N = 0$ oscillator shell, the $2s_{1/2}$ stemming from the $N = 2$ oscillator shell, or the $1p_{3/2}$ and $2p_{3/2}$ stemming from the $N = 1, 3$ oscillator shells, respectively. Table 1 gives a summary of the shells, together with the number of nucleons each state can hold. For a more detailled description the reader is referred to the texts given near the beginning of the chapter.

Table 1 Shell model states for each oscillator shell, their occupancies and the resulting shell closures. Up to $N = 20$ the magic numbers are correctly reproduced.

N	States	Occupancy	Total
0	$1s_{1/2}$	2	2
1	$1p_{1/2}$, $1p_{3/2}$	$2+4=6$	8
2	$2s_{1/2}$, $1d_{3/2}$, $1d_{5/2}$	$2+4+6=12$	20
3	$2p_{1/2}$, $2p_{3/2}$, $1f_{5/2}$, $1f_{7/2}$	$2+4+6+8=20$	40
4	$3s_{1/2}$, $2d_{3/2}$,$2d_{5/2}$, $1g_{7/2}$, $1g_{9/2}$	$2+4+6+8+10=30$	70
5	$3p_{1/2}$, $3p_{3/2}$, $2f_{5/2}$, $2f_{7/2}$, $1h_{9/2}$, $1h_{11/2}$	$2+4+6+8+10+12=42$	112
6	$4s_{1/2}$, $3d_{3/2}$,$3d_{5/2}$, $2g_{7/2}$, $2g_{9/2}$, $1i_{11_2}$, $1i_{13/2}$	$2+4+6+8+10+12+14=56$	168

The closed oscillator shells coincide with the lower magic numbers $N = Z = 2, 8, 20$ but fail to reproduce the experimentally observed ones at higher numbers. The missing ingredient is a strong and attractive spin-orbit interaction, first proposed by Goeppert-Mayer and Jensen in 1948 [1, 2]. The spin-orbit interaction is largest near the nuclear surface and is often written as

$$V_{ls} \propto \frac{\mathrm{d}\, V(r)}{\mathrm{d}\, r} \hat{l} \cdot \hat{s} \tag{11}$$

where $V(r)$ is the radial part of the nuclear potential. This is illustrated in Fig. 6, where a Woods-Saxon shape was assumed for the nuclear potential.

We show in Eq. 12 how one can evaluate the magnitude of the term $l \cdot s$ to be

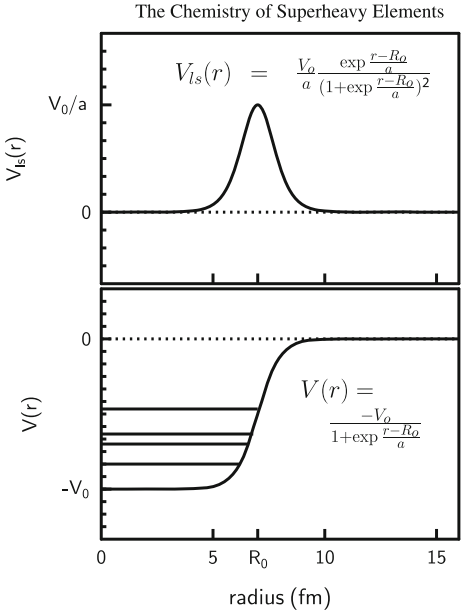

Fig. 6 Schematic representation of the shell model potential and the spin-orbit interaction (*top*) usually taken as proportional to the derivative of the potential, illustrated via a Woods-Saxon potential (*bottom*) with a nuclear radius R_0 and a surface diffuseness a. A few nuclear levels inside the potential are schematically indicated. It is then obvious that the spin-orbit interaction mainly acts near the surface of the nucleus

$$l.s = \begin{cases} l+1 & \text{for} \quad j = l - 1/2 \\ -l & \text{for} \quad j = l + 1/2 \end{cases} \tag{12}$$

This means that the state with the larger j will get lowered, while the state with the smaller j gets raised in energy, resulting in a spin-orbit splitting proportional to $2l + 1$. The magic numbers are now easily explained. The spin orbit interaction acting on the first $f_{5/2}$–$f_{7/2}$ pair in the $N = 3$ oscillator shell lowers the $f_{7/2}$ state to lie energetically between the states of the second oscillator shell and the remaining states in the third shell. As it can hold eight nucleons, it forms the $N = Z = 28$ subshell. The shell at 50 is formed in a similar way: The spin-orbit interaction lowers the $g_{9/2}$ state to lie energetically close to the states in the $N = 3$ shell, adding its 10 nucleons to the 40 already present. The shell at 82 is formed by lowering the $h_{11/2}$ state into the lower shell, and so on. This is illustrated schematically in Fig. 5 where an additional term proportional to l^2 is included. This term simulates a flattening of the potential at small radii and thus gives a better match of the harmonic oscillator potential to the potential of the nucleus, which is better described by a Woods-Saxon shape with a flat bottom.

In order to gain an understanding of the situation for superheavy elements the 82–126 shell is redrawn in Fig. 7, where the effect of large and small spin orbit interaction is illustrated. The predicted shell closure at 114 is realised if a large spin-orbit interaction gives a large splitting between the $2f_{5/2}$ and $2f_{7/2}$ states, and the $1i_{13/2}$ state lies well below the $2f_{5/2}$ state. It is easy to see how a shift in the energy centroids of the various components and a change in spin-orbit interaction strength will lead to the opening and closing of shells at $Z = 114$ and $Z = 120$, leaving only

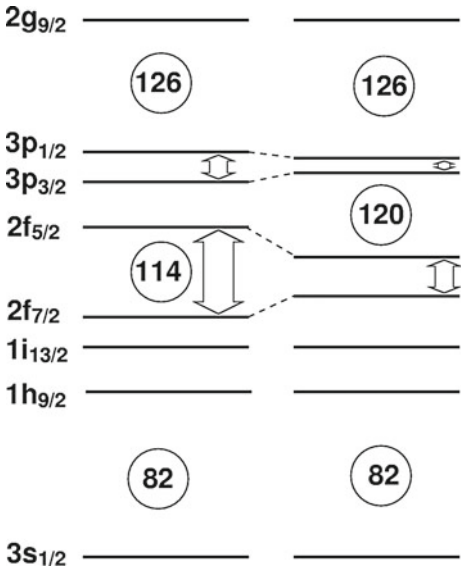

Fig. 7 Shell model level ordering resulting from large (*left*) and small (*right*) spin orbit interaction. The opening and closing of shells at 114 and 120 is clearly seen. Figure reproduced from [22] with permission

$Z = 126$ as a large shell gap. This uncertainty of the positions of the spherical orbitals lies at the heart of the problem of locating the next spherical shell closure.

One word of caution. It is tempting to infer a shell closure from the existence of a large energy gap between levels alone. While this is generally a good approximation at low masses, the high degeneracy of the high-l orbitals starts to play an increasingly important role in heavier nuclei. Stability is not primarily associated with the large energy gap, but really with regions of low level density. This leads to a softening of the magicity illustrated in Fig. 8 [23–25]. Here the shell correction energy is compared for several realistic model calculations for the Sn region (top) and the superheavy region (bottom). In the Sn region the magic numbers 50 and 82 attract extra binding energy, with the doubly magic character clearly in evidence. For the superheavy region the picture is very different. Entire regions of the nuclear chart gain stability through shell effects, leading to much broader "islands" of stability.

2.4 The Deformed Shell Model

Most nuclei are well deformed. From a single particle point of view this means that the total energy of the nucleus can be minimized by arranging the nucleons in a deformed configuration. If the energy gain in this configuration is greater than the energy required to deform the bulk of the nucleus (as seen in the LDM), then the ground state will be deformed and the resulting deformed mean field splits the degeneracy of the spherical single particle levels. The Nilsson model [26] is commonly used to extend the shell model to deformed systems.

If the nucleus deforms axially, the spherical states will split into $(2j + 1)/2$ levels, each still with twofold degeneracy. It is instructive to trace the breaking of the degeneracy back to first principles, namely that the nuclear interaction is short range and attractive. In a deformed nucleus it can therefore be expected that the overlap of the nuclear wavefunction with the bulk of the nucleus determines the energy gain.

Consider a prolate, axially symmetric nucleus with the quantization axis identical to the nuclear symmetry axis. A $g_{9/2}$ proton orbits the nucleus and can occupy any of the m-substates associated with $j = 9/2$, i.e. $\pm 9/2$, $\pm 7/2$, $\pm 5/2$, $\pm 3/2$ and $\pm 1/2$. The projection m of the total angular momentum is usually abbreviated with the letter Ω (see Fig. 9). If we compare the states with $\Omega = 9/2$ and $\Omega = 1/2$ then the former state has j aligned with the nuclear symmetry axis, which means that the nucleon orbits in an equatorial plane nearly perpendicular to that axis. The prolate deformation then means that the nucleon has a small overlap with the other nucleons constituting the nuclear bulk. The $\Omega = 1/2$ state on the other hand has j oriented nearly perpendicular to the symmetry axis, which means that the nucleon occupies a polar orbit resulting in a large overlap with the bulk. It therefore feels a much larger attractive force than the $\Omega = 9/2$ state, and its energy is consequently lowered relative to the $\Omega = 9/2$ state. The remaining states will

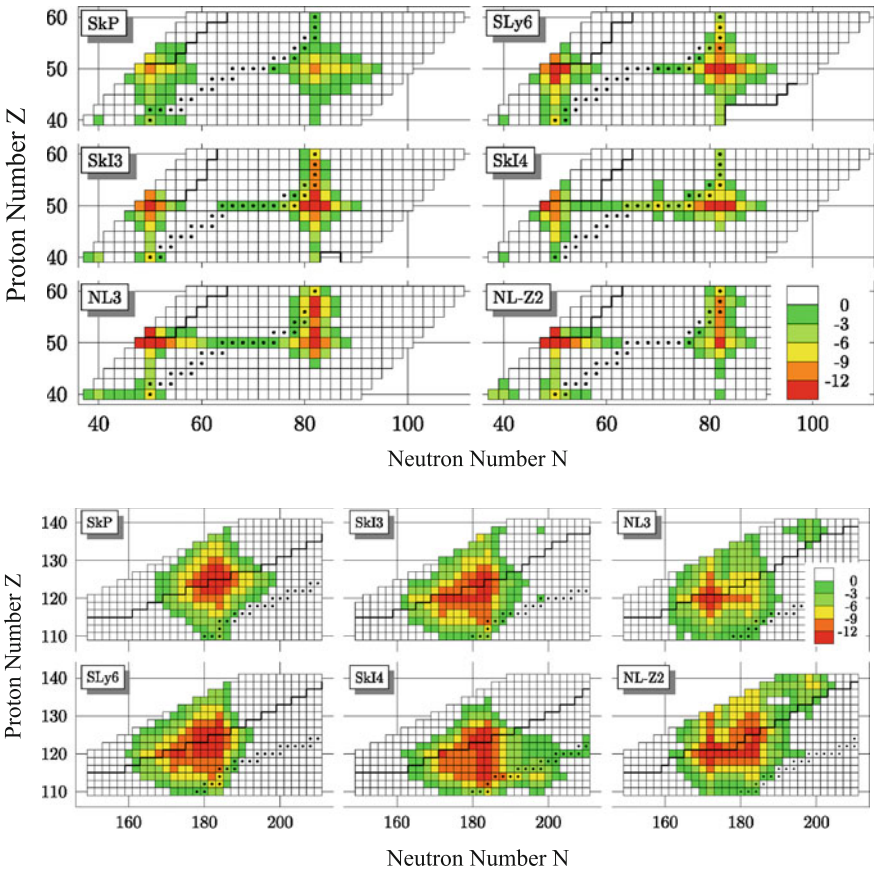

Fig. 8 Shell correction energies for the Sn region (*top*) and the superheavy region (*bottom*) calculated with various interactions. Increasing shell correction energies are colour coded from green (*lowest*) to red (*highest*). The shell stabilization closely traces the magic numbers around Sn while larger islands of stability are formed in the superheavy region. Adapted from [23]

have intermediate energies increasing with increasing Ω, and the resulting levels will still be twofold degenerate in $\pm\Omega$. In the (rare) case of oblate deformation the situation is precisely the opposite, with the nucleon with the largest Ω now circling an equatorial bulge, resulting in this state being lowered by the largest amount.

A complication arises from the possibility of mixing. In a deformed system the states with the same Ω and the same parity can mix leading to a physical state with contributions from several spherical states. For very small and very large deformations this mixing is typically small with a single configuration dominating the wave function. However, for intermediate deformations this mixing can lead to deformed wave functions with large contributions from more than one spherical state. In the Nilsson model the states are therefore labelled with "asymptotic quantum numbers", which become exact only in the limit of very large deformations.

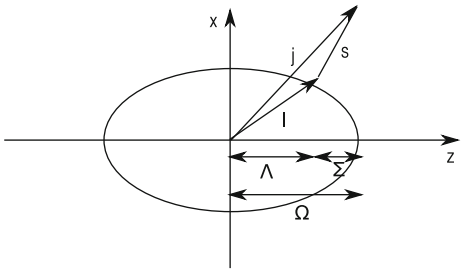

Fig. 9 Schematic representation of the angular momenta in deformed odd mass nuclei and their projections onto the nuclear symmetry axis

The asymptotic labels are given in the form $\Omega^{\pi}[N, n_z, \Lambda]$, see Fig. 9. Here Ω is the projection of the total angular momentum j onto the nuclear symmetry axis, N is the main oscillator quantum number, $\pi = (-1)^N$ is the parity of the state, Λ is the projection of the orbital angular momentum onto the nuclear symmetry axis and n_z counts the number of radial nodes in the wave function. This notation will be used throughout the chapter.

3 Rotational Structure of Nuclei

A spherical nucleus cannot rotate. In order to rotate, the wave function of the system rotated by a small angle α must be distinguishable from the non-rotated wave function. In a spherical system that is impossible and consequently no rotational bands are observed built on spherical configurations, such as the ground states of doubly magic nuclei. A deformed quantum system on the other hand will exhibit rotational behavior. The excitation energy required to set a nucleus rotating is very small compared to the energy required to excite vibrations. Typical excitation energies of the first rotational 2^+ state in superheavy nuclei are only of the order of 40–50 keV. The amount of information available on excited states in superheavy nuclei is rather limited, but has been steadily growing in the last decade. Figure 10 summarises all available information on excited states in nuclei with $Z \geq 96$. While individual rotational levels are often populated in alpha decay, the only rotational bands consisting of several levels observed in nuclei beyond Fm stem from in-beam measurements [27]. It is also obvious that the ground state spins and therefore the ground state configurations are not well determined. The last direct measurement of the ground state spin is in ^{253}Es, where the spin $7/2^+$ was measured directly using laser spectroscopy [28]. All other spins are inferred from systematics and alpha decay chains (see Sect. 5.4).

In this section we first introduce the quantum numbers, notations and conventions usually associated with the description of rotational bands. Then we look at transitions within rotational bands and classify rotational bands according to their K quantum number. We then turn our attention to the influence the

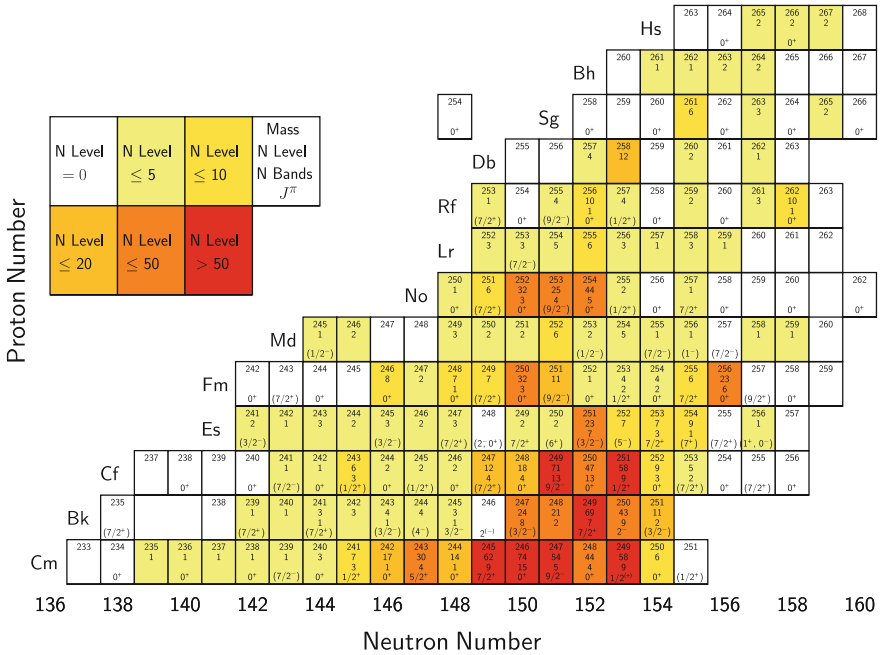

Fig. 10 Summary of experimental information available in the ENSDF data base at the end of 2011 for nuclei from Cm to Hs. The ground state spin, number of known excited levels and number of rotational bands observed are given. In order to help with readability no isotopes with $N > 160$ were included. This figure is an updated version of the one given in [27]

underlying single-particle structure has on the rotational bands, and how this can be used to deduce information about the nucleons responsible. Finally we look at the experimental methods aimed at studying superheavy nuclei.

3.1 Rotational Bands in Even-Even Nuclei

For a definition of the various quantum numbers needed to describe rotational bands we refer to Fig. 11, where we show a well-deformed axially symmetric even-even nucleus. The coordinate axes in the lab system will be labeled with x, y, and z. The coordinate axes in the intrinsic system (in which the nucleus is stationary) are labeled with 1, 2, and 3, with the 3-axis pointing along the symmetry axis.

An intrinsic excitation upon which the rotational band is built, such as, e.g., a vibration or a two-quasiparticle excitation, can be present and is characterized by the projection of its intrinsic angular momentum I on the nuclear symmetry axis. This projection is called the K quantum number. The parity π of the band is also determined entirely by the intrinsic configuration. The entire system can then

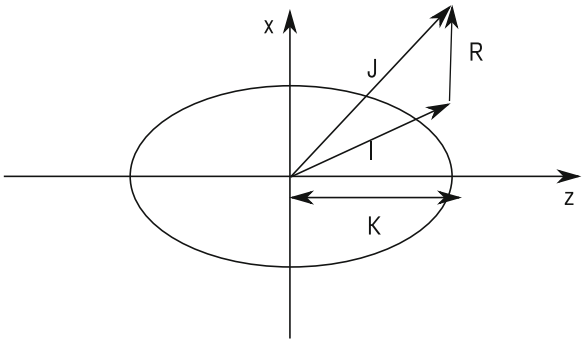

Fig. 11 Schematic representation of the angular momenta in the nucleus. On *top* of an intrinsic excitation with angular momentum I and projection K a collective rotation can be built with orbital angular momentum R. The total angular momentum of the nucleus is J, and all levels in the resulting rotational band have the same K quantum number

exhibit collective rotation around an axis perpendicular to the nuclear symmetry axis with angular momentum R. The total angular momentum J is therefore given by the (quantum mechanically correct) vector sum of $J = I + R$. It is immediately clear that an increase in R can change the length of J, but not K. This has two consequences: A band built on the intrinsic configuration (I, K) will consist of states all of which share the same K quantum number, which is used to characterize the band. Secondly a rotational band with $K > 0$ can not contain a state with angular momentum $J < K$, providing the experimentalist with an easy way to identify K typically as the spin of the bandhead, i.e. the energetically lowest member of the band. The only exception to this rule are negative parity bands with $K = 0$ which have a bandhead spin of $J^\pi = 1^-$.

Figure 12 shows the level scheme of the nucleus ^{254}No. A number of rotational bands is seen, with very different characteristics. The ground state rotational band consists of states with even spins connected by electric quadrupole (E2) transitions. One short band is seen built on a 3^+ state consisting of a characteristic pattern of states with all integer spins greater than three. The sequence 3–5–7 forms one rotational band connected by stretched E2 transitions, as does the sequence 4–6–8. Additionally there are interband transitions $5 \rightarrow 4, 4 \rightarrow 3$ etc. For these transitions both electric quadrupole (E2) and magnetic dipole (M1) transitions are allowed to contribute. The branching ratios of these low-energy transitions carry a lot of information about the underlying structure, which we will exploit in Sect. 4.3. Other bands are seen, and the transitions linking excited bands into the ground state band are indicated. We will return to this level scheme throughout the section as a standard example. In general, rotations are described through the Hamilton operator

$$\hat{H} = \frac{\hbar^2}{2\Theta}\hat{J}^2 \tag{13}$$

where we use Θ as the moment of inertia. This operator has eigenvalues

$$E(J) = \frac{\hbar^2}{2\Theta}J(J+1)\ . \tag{14}$$

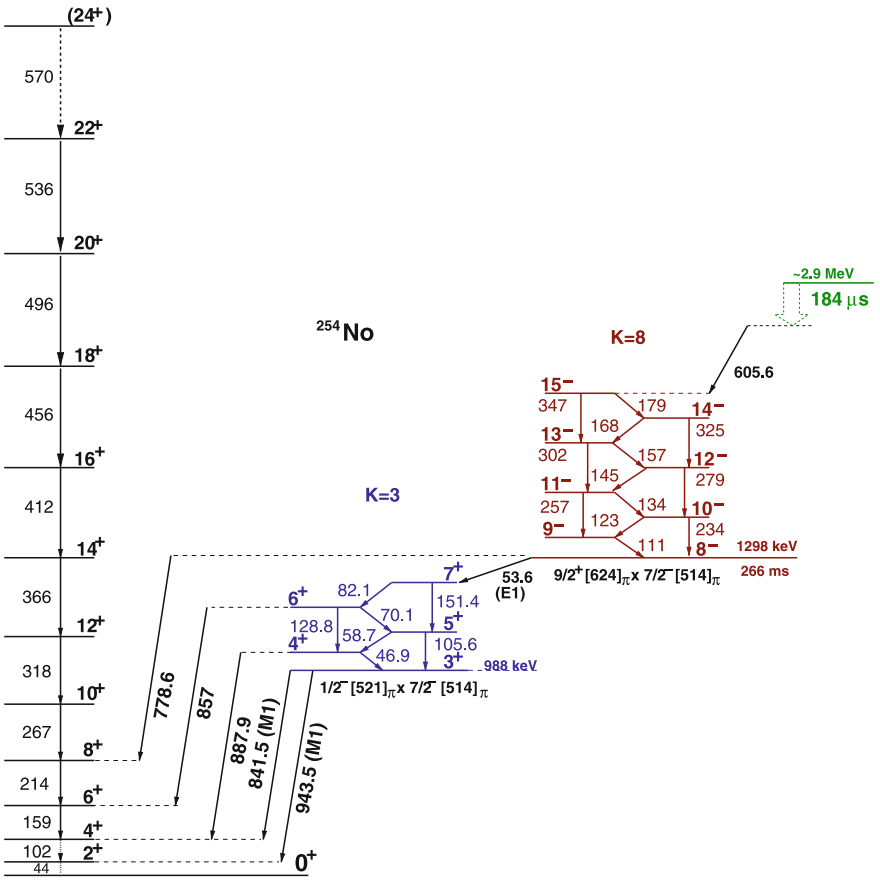

Fig. 12 Level scheme for ^{254}No. The band built on the ground state with spin 0 and $K = 0$ consists of a sequence of stretched $E2$ transitions, while both excited bands are built on configurations with $K > 0$ and consist of both stretched E2 and mixed E2/M1 transitions. The observed branching ratios can be used to determine the underlying nuclear configuration. The numbers give the assigned spins and the energies of the transitions in keV

This leads to a spacing between consecutive levels of the same band of

$$E_T(J \to J-2) = \frac{\hbar^2}{2\Theta}[J(J+1) - (J-2)(J-1)] = \frac{\hbar^2}{\Theta}(2J-1) \tag{15}$$

leading to the characteristic "comb structure" in the gamma spectrum.

We will first restrict ourselves to rotational bands with $K = 0$, such as the ground state rotational bands (gsb) in even-even nuclei. From the level scheme in Fig. 12 we see that the gsb consists solely of levels with even angular momentum, with increasing energetic spacing between them.

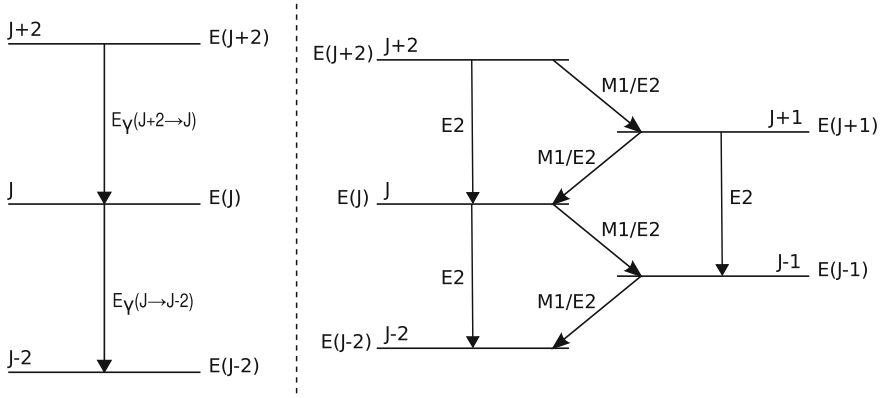

Fig. 13 Definition of labels for transitions in a rotational band. On the *left* we show the case for a single rotational band, e.g., the ground state rotational band in an even-even nucleus. Two stretched electric quadrupole ($E2$) transitions populate and depopulate the band member with angular momentum J. The transition energies E_γ and the level energies $E(J)$ are indicated. On the *right* hand side we show the more frequent case of two strongly coupled bands. Stretched $E2$ transitions connect the members of each band, while the bands are connected by interband transitions of mixed $M1/E2$ character. The branching ratios between the mixed interband transitions and the stretched intraband $E2$ transitions are sensitive to the g-factor of the band-head configuration

To understand the lack of odd spin states we have to look closer at the underlying symmetry. Assume the nucleus has rotated through 180°. From the symmery of the nucleus it is clear that this wave function is now identical to the unrotated one: $|J> = \mathscr{R}(180°)|J>$. However, a closer inspection of the Eigenfunctions (the spherical harmonic functions) of the rotational Hamilton operator shows that they obey the relation $(-1)^J|J> = \mathscr{R}(180°)|J>$. For even spins this is allowed, for odd spins this leads to the condition $|J> = -|J>$, which can only be fulfilled by a wave function identical to 0 everywhere: i.e. no such level can exist. As soon as the symmetry is broken, e.g., by having $K > 0$, this contradiction is removed, and *all* possible values of the angular momentum are realized in the band. However, a band with only even spins immediately leads to the conclusion $K = 0$.

We can now attempt to extract the moment of inertia (MoI) from the observed levels. For this it is useful to define the levels, angular momenta and energies as shown in Fig. 13.

Furthermore, to avoid cluttering the discussion, we restrict ourselves to electric quadrupole transitions and we shall be guided by the relations between energy E, angular frequency ω and moment of inertia Θ found for classical rotations:

$$J = \Theta\omega \qquad \text{and} \qquad E_{rot} = \tfrac{1}{2}\Theta\omega^2 = \tfrac{1}{2}J\omega = \frac{J^2}{2\Theta} \ . \tag{16}$$

The angular frequency can then be found for discrete electric quadrupole transitions as

$$\omega = \frac{J}{\Theta} = \frac{dE}{dJ} \simeq \frac{\Delta E}{\Delta J} = \frac{E_\gamma}{2} \ . \tag{17}$$

We are interested in the MoI that we can attribute to the state with spin J. There are two main ways to extract the MoI from the observed discrete transitions [29]. The kinetic MoI $\Im^{(1)}(J)$ can be extracted from the relationship

$$\frac{\Delta E}{\Delta J} = \frac{1}{2\Theta}[J(J+1) - (J-2)(J-1)] = \frac{2J-1}{2\Theta} = \omega \tag{18}$$

as

$$\Theta = \Im^{(1)} = \frac{2J-1}{2\omega} = \frac{2J-1}{E_\gamma} \ . \tag{19}$$

This form has the advantage that it can easily be assigned to a level from which a single gamma transition is observed. The disadvantage is that the angular momentum of the level has to be known. To get around this limitation it is often convenient to use the dynamic moment of inertia $\Im^{(2)}(J)$ obtained from the relation

$$\begin{aligned} \Im^{(2)} &= \frac{\Delta J}{\Delta \omega} = \frac{2}{\omega(J+2 \to J) - \omega(J \to J-2)} \\ &= \frac{4}{E_\gamma(J+2 \to J) - E_\gamma(J \to J-2)} \end{aligned} \tag{20}$$

In this form one requires no knowledge of the angular momentum, but one needs to have observed two transitions feeding and depopulating the state of interest. One can easily verify that both expressions give identical results for a rigid rotor. However, the rotational properties of a nucleus are not those of a rigid body, but more akin to a nonrotating superfluid [30], which leads to deviations from the rigid rotor results. In particular one finds that the MoI is typically only about half that of a rigid rotor and that the MoI increases as one breaks pairs of nucleons. At the highest excitation energies where several pairs of nucleons have been broken, the MoI approaches a significant fraction of that of the rigid body.

A number of approaches are used throughout the literature to describe this variable MoI. We shall use the one proposed by Harris [31] where the dynamic MoI is expanded as a power series in ω

$$\Im^{(2)} = A + B\omega^2 + C\omega^4 + \ldots \tag{21}$$

The angular momentum of a state can then be found (up to a constant) through integration

$$I = \int \Im^{(2)} d\omega = A\omega + B\omega^3 + \cdots + const. \tag{22}$$

For even-even ground state bands the additive constant is $1/2$, but in general it is not straightforward to deduce reliable spins through this method [29]. However, this approach is often useful to give an indication of the expected angular momentum and can be used in conjunction with other experimental constraints to construct a coherent level scheme.

The Harris fit is also useful to extrapolate a rotational band to unobserved transitions. In the transfermium region the lowest transitions are typically so highly converted that they can not be observed through gamma spectroscopy (see the discussion in Sect. 5). In these cases it is useful to extract the Harris parameters A and B from a fit to the observed MoIs in the ground state rotational band, and solve for the frequency corresponding to the angular momentum of the missing state. In this way the $4^+ \rightarrow 2^+$ and $2^+ \rightarrow 0^+$ energies of various No and Fm nuclei were extracted [27].

3.2 Backbending and Alignment

So far we have treated the rotating nucleus as a body without internal structure, a description that ignores the fact that the nucleus is made up of nucleons which themselves have angular momentum and will therefore interact with the rotating frame via the Coriolis interaction. The Coriolis interaction will act in a way to align the angular momenta of all components of the system with that of the collective rotation. The net effect is one where the nucleus can generate a higher angular momentum without having to spin faster, simply by breaking a pair of nucleons and adding the intrinsic angular momentum of these nucleons to its collective rotation. This effect shows up in a plot of angular momentum versus rotational frequency as a distinctive backbend.

The Coriolis force in a nucleus rotating with angular momentum R acts on a pair of particles with single particle spins j coupled to a pair with total spin $J = 0$. In this pair the nucleons occupy time reversed orbits, i.e. their angular momentum vectors point in opposite directions. It is now clear that the Coriolis force will act differently on the two nucleons trying to align both spins with the collective rotation, effectively breaking the pair and adding $2j$ to the total angular momentum. From the shape of the Coriolis force it is clear that this will happen to those nucleons with the largest spins first, e.g., in the well deformed region around nobelium these are the $j_{15/2}$ neutrons and the $i_{13/2}$ protons.

Figure 14 shows a collection of the measured dynamic MoIs for Pu, Cm, Cf, Fm and No nuclei showing distinct upbends around a rotational frequency of 200 keV in all nuclei, yet it also shows individual differences between nuclei. If we examine the cases of ^{252}No and ^{254}No, we note that the MoI increases more steeply in ^{252}No than in ^{254}No [32]. This behavior can be traced directly to the underlying nucleon configurations and through comparisons with model calculations one sees that in both cases an alignment of $i_{13/2}$ protons and $j_{15/2}$ neutrons is expected. However,

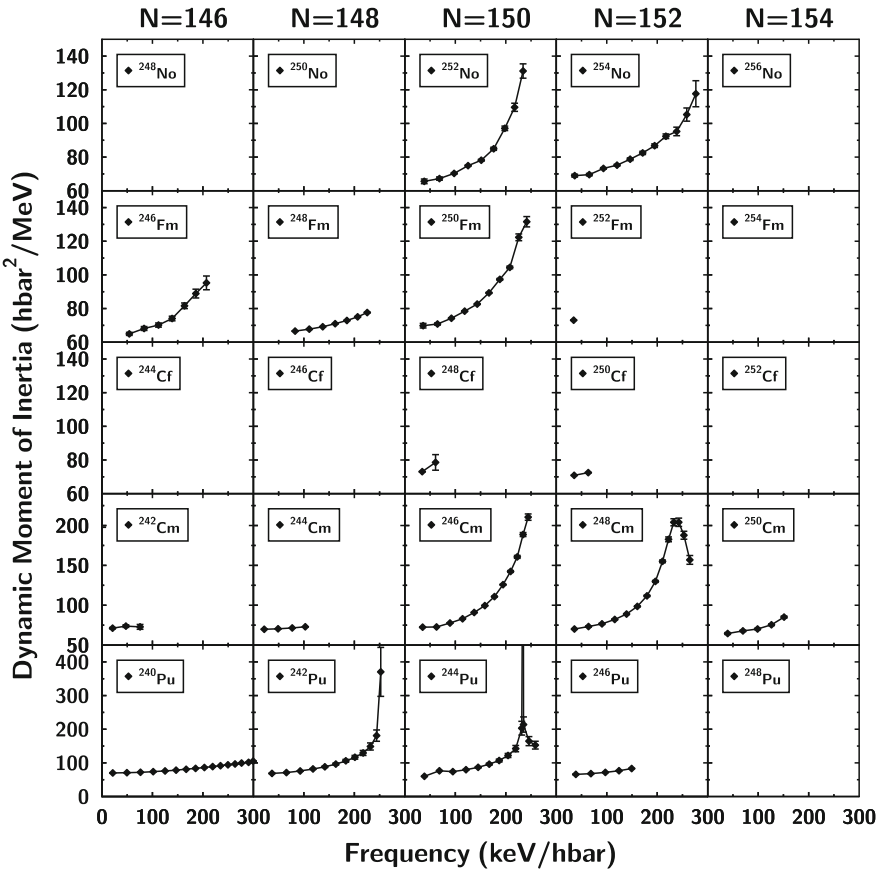

Fig. 14 Moments of inertia for Pu, Cm, Cf, Fm and No nuclei. Upbends around a frequency of 200–300 keV show the alignment of pairs of nucleons with the highest orbital angular momenta (see text). Figure adapted from [27]

in ^{254}No this alignment is expected to occur at the same frequencey, while in ^{252}No the $j_{15/2}$ neutrons are expected to align first. Thus in ^{254}No the available rotational energy is required to account for the breaking and alignment of both pairs and consequently the process is spread out over a larger number of transitions in ^{254}No. This sensitivity of the MoI to the underlying shell structure means that one can get a surprisingly accurate experimental handle on the shell structure simply by observing a number of rotational states, the energies of which are easily extracted with good accuracy in modern gamma ray spectrometers.

The energies of transitions in rotational bands can further be exploited to extract the aligned angular momentum to directly measure the spin of the particle aligning. This requires measurements that go beyond the alignment frequency,

which have not yet been possible for nobelium nuclei. However, in well deformed rare earth nuclei long rotational bands often with more than one backbend can be found.

4 Single Particle Structure of the Nucleus

The ultimate goal of any nuclear structure investigation on a heavy nucleus is to learn something about the underlying single particle structure that is responsible for the added stability at the top end of the Periodic Table. This endeavor is made more complicated by the fact that the single particle structure changes significantly with deformation. As deformed, heavy actinide nuclei are currently providing the bulk of the experimental data on single particle excitations, it is important to understand how one can draw conclusions about spherical levels from a study of deformed ones. This section gives an overview of single particle and quasi-particle states, g-factors and nuclear isomerism.

4.1 Pairing and Quasi Particle States

The shell model describes the nucleus as a system of independent particles coupled by a residual interaction. This residual interaction is generally complicated, but in the case of particles with the same spin j it takes a particularly simple form. Figure 15 shows the schematic level scheme of a pair of $h_{9/2}$ protons, compared with the experimentally observed level scheme of ^{210}Po, which, in the shell model, is described as two $h_{9/2}$ protons outside a closed ^{208}Pb core. In general this energy gained through pairing leads to all nucleons in the nucleus being paired

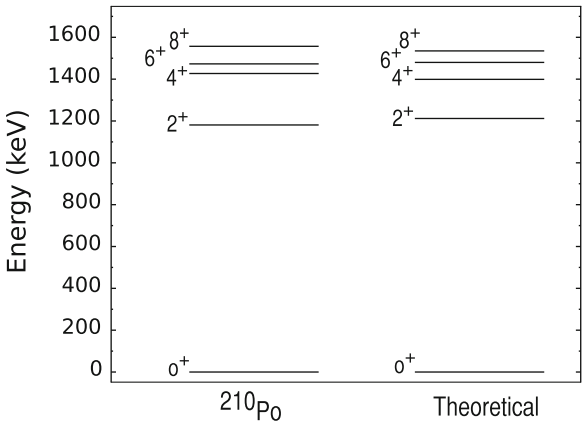

Fig. 15 Schematic level scheme for a pair of $h_{9/2}$ protons (*right*) compared to the low lying levels in ^{210}Po (*left*)

and exciting configurations will involve the breaking of pairs. The situation becomes more complicated in deformed nuclei where the shells lose their degeneracy in j. The minimal energy for the ground state of such nuclei then usually involves a probabilistic distribution of particles across a large number of states, and the description of excitations must take this complicated ground state into account.

The situation can be greatly simplified by translating into a basis where we replace a system of strongly interacting particles by one of non-interacting quasiparticles by means of the Bogoliubov transformation. The details shall be left to the reader to find in one of the many undergraduate textbooks available (e.g., [8–10]), here we shall concentrate on the interpretation.

The Hamilton operator can be written in three terms:

$$\hat{H} = \hat{H}_0 + \hat{V}_{pair} - \lambda \hat{N} \, . \tag{23}$$

The first term accounts for the energy of the independent particles making up the nucleus, the second term describes the interaction between two pairs of particles, and the third term is required to keep the particle number in the nucleus correct. Thus the problem must be solved under the condition that the expectation value of the particle number coincides with the number of particles in the nucleus.

The effect of this transformation is the emergence of quasiparticles which can now take the roles of the independent particles. The correlations introduced by the pairing interaction have been taken into account, at the price of somewhat modified energies of the quasiparticle states. When solving the BCS[1] equations we also find a gap parameter Δ, which in heavy nuclei typically has values $\Delta \simeq 0.5$–0.8 MeV, and is associated with the strength of the particle-hole correlations near the Fermi level, which in this pairing picture is given by the parameter λ.

If the original single particle energies are denoted by ε_i, the Fermi level by λ and the gap parameter Δ, the energy of the corresponding quasiparticle is given by

$$E_i = \sqrt{(\varepsilon_i - \lambda)^2 + \Delta^2} \tag{24}$$

A particle-hole excitation in the presence of pairing can now easily be described by a two-quasiparticle excitation, where the excitation energy of the final state is simply given by the sum of the quasiparticle energies

$$\Delta E = E_i + E_j = \sqrt{(\varepsilon_i - \lambda)^2 + \Delta^2} + \sqrt{(\varepsilon_j - \lambda)^2 + \Delta^2} \geq 2\Delta \, . \tag{25}$$

For energies far from the Fermi level this reduces to the original energy of the particle and the hole, but for excitations near the Fermi surface a minimum energy of 2Δ is required. This is easily seen in Fig. 16 where the low-lying levels of

[1] Named after the scientists who first used this type of pairing to explain superconductivity, J Bardeen, L N Cooper and J R Schrieffer.

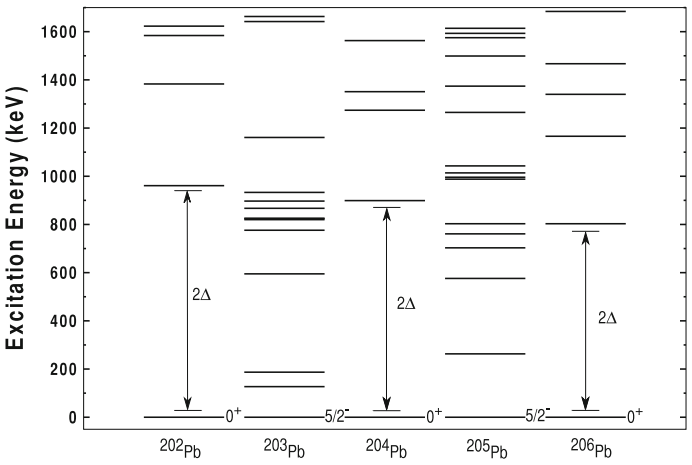

Fig. 16 Low-lying excitation spectra of Pb isotopes. The effects of the pairing interaction are clearly seen in the even isotopes

$^{202-206}$Pb are plotted. In even nuclei the pairing gap is clearly visible, whereas in odd nuclei the single particle spectrum can start at much lower excitation energies.

In well deformed nuclei the two-quasiparticle states retain another property, namely the projection of the contributing spins on the nuclear symmetry axis, K. This means the occurrence of states with large values of K becomes common and can often lead to K-isomerism, which will be discussed later.

4.2 Nuclear g-Factors

Both protons and neutrons carry a magnetic moment. While this is immediately obvious for a rotating charge distribution such as the proton, it is important to remember that this magnetic moment is generated by the charged quarks making up the nucleons. Therefore all constituent nucleons carry a magnetic moment in addition to the bulk magnetic moment of the rotating nucleus itself. The magnetic properties of a state therefore provide us with an experimental handle that we can use to determine the underlying single particle configuration. For a nucleus consisting of hundreds of nucleons this looks to be a daunting task. However, the situation is greatly simplified through the effects of pairing, namely the fact that the nuclear magnetic moment of a pair of nucleons coupled to spin $J = 0$ vanishes. This means that an even-even nucleus has no magnetic moment in its ground state, and the magnetic moment of the ground state of an odd mass nucleus is determined by the magnetic moment of the unpaired particle.

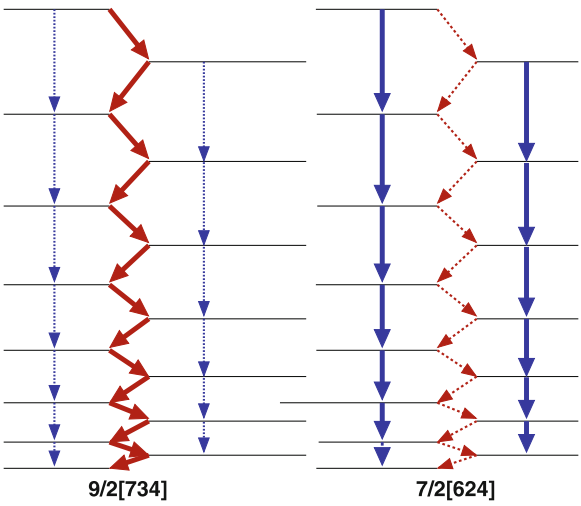

Fig. 17 Predicted intensity pattern in the ground state band of ^{253}No for two different ground state configurations. For the $9/2$ configuration $M1$ interband transitions are dominant whereas for the $7/2$ configuration the $E2$ transitions carry the majority of the intensity. Adapted from [33]

The magnetic moment μ of a spinning charge distribution is proportional to the angular momentum, $\boldsymbol{j}$. The proportionality is given by the g-factor, and the magnetic moment is measured in nuclear magnetons $\mu_N = e\hbar/2m_p$:

$$\mu = g\boldsymbol{j}\,\mu_N\ . \tag{26}$$

The situation is complicated for nucleons as they carry both orbital angular momentum and intrinsic spin, leading to complex expressions for the g-factors. However, they can be calculated readily, and then compared to the observed values to make structural assignments. We will refer to the g-factors due to the individual nucleons as g_K, and to the g-factor due to the nucleus rotating as a whole as g_R. Since only the protons contribute to the magnetic moment of the rotating nucleus we use $g_R \simeq Z/A$ as a good approximation [30].

The experimental handle is then provided by the gamma ray branching ratios between $M1$ and $E2$ transitions in a rotational band built on a state with a g-factor g_K. The intensities of the magnetic dipole transitions are proportional to $(g_K - g_R)^2$, while those of the electric quadrupole transitions are proportional to the electric quadrupole moment Q^2, which does not tend to vary greatly between bands in a given nucleus as it is associated predominantly with the shape of the nucleus as a whole.

Using the definitions of spins and transitions shown in Fig. 13 we find that the branching ratio for gamma transitions depopulating the level with spin J is proportional to $[(g_K - g_R)/Q]^2$, and thus the single particle configuration of the state the band is built upon can be determined by measuring gamma branching ratios in a rotational band. This is illustrated in Fig. 17 where the expected behaviour of the ground state rotational band in ^{253}No is plotted for two different ground state configurations. The $9/2^-[734]$ configuration has a g-factor $g_K = -0.24$ while the

$7/2^+[624]$ configuration has $g_K = 0.28$. Together with $g_R = Z/A \simeq 0.4$ the branching ratios should favour $M1$ transitions for the $9/2^-[734]$ configuration and $E2$ transitions for the $7/2^+[624]$ configuration. Indeed experimental branching ratios favour the $9/2^-$ configuration [34].

4.3 Nuclear Isomers

The half-life of excited nuclear states is typically of the order of picoseconds. However, sometimes one can observe states with significantly longer half-lives, nuclear isomers. In extreme cases the half-life of the isomeric state can exceed the half-life of the ground state. Take as an example the case of ^{180}Ta. This is one of the rarest isotopes that can be found in an isomeric state naturally on earth, where it is to all intents and purposes stable with a half-life $T_{1/2} > 1.2 \times 10^{15}$ y. However, its ground state decays rapidly with a half-life of only $T_{1/2} = 8.125$ h.

To explain isomerism we turn to Fermi's Golden Rule which relates the transition rate to the wave functions of the initial and any final states as well as the density of final states in a given energy interval. In short, a decay can only happen if a suitable final state exists, and, if it does, the transition rate is higher the more the wave function of the final state resembles that of the initial state. We therefore expect isomers to occur in several classes:

Shape Isomers can be found in the second minimum of the fission barriers of actinides. If the nucleus is prepared in the lowest state in the second minimum it is much more deformed than in any of the states in the first minimum. Thus any transition out of the second minimum will require the rearranging of all nucleons, which leads to the observed very small matrix elements and thus the formation of an isomeric state. These isomers are also known as fission isomers.

Spin traps are formed by states which have no states with comparable spins and parities at lower energy that they can decay to. The gamma decay selection rules then lead to very long half-lives as the decays have to proceed through transitions with very high multipolarity. This situation is common in odd–odd nuclei. The above example of ^{180}Ta is such a case where the isomer at an excitation energy of 75 keV above the ground state has a spin $J^\pi = 9^-$ while the ground state itself has spin $J^\pi = 1^+$ requiring an $M8$ transition between them.

K Isomers are the nuclear analogues to the bicycle. They form when the K quantum number has to change during a transition, which requires a change of the orientation of the angular momentum vector. K isomers are found, e.g., when two quasiparticle states with large K form as the lowest quasiparticle excitations. This situation is the most common one in the regions around Hf and No [41].

It is instructive to look at the occurrence of isomers in heavy nuclei. Figure 18 shows the longest lived isomers known in all nuclei from Pb onwards [35]. The heaviest listed nucleus is ^{270}Ds which has an isomer with a half-life $T_{1/2} = 6.0^{+8.2}_{-2.2}$ ms, while its ground state has a half-life $T_{1/2} = 100^{+140}_{-40}$ μs [42].

Fig. 18 Longest lived isomer known in all nuclei above $Z \geq 82$. The size of the symbols indicate half-lives. Figure reproduced from [35] with permission. Copyright 2011 Oldenburg Wissenschaftsverlag GmbH

To us isomerism raises an important question: "Can nuclear isomerism lead to the natural occurrence of superheavy elements in an isomeric state?" This has been a question of much interest recently, see, e.g., [41]. If isomeric states in the region around hafnium and tantalum can live for geological timescales, why should similar isomers not occur in the superheavy region? The neutron numbers in the Hf region are between 100 and 110 with the last neutrons occupying the same orbitals occupied by protons in heavy actinide and transactinide nuclei. Thus conditions in the superheavy region may very well allow long-lived isomeric states that give some hope to find superheavy elements in nature.

4.4 Deformed Gaps

The main focus on shell gaps in the study of superheavy elements has always been the next spherical shell closure for protons and neutrons. However, since the majority of heavy and superheavy nuclei are well deformed, it is also important to understand the effects of deformed shell closures in lighter systems. Here too doubly magic systems can be found, albeit with a different understanding of the magic character.

In Sect. 2.3 we discussed the effect of large energy gaps (see, e.g., Fig. 8) and found that the magic character was not so much down to the large energy gap between two levels, but ultimately the important quantity was the level density, with a low level density leading to extra stability. In the deformed shell model the degeneracy in total angular momentum j is lifted and the state j splits into $(j + 1/2)$ individual components characterized by the projection on the nuclear

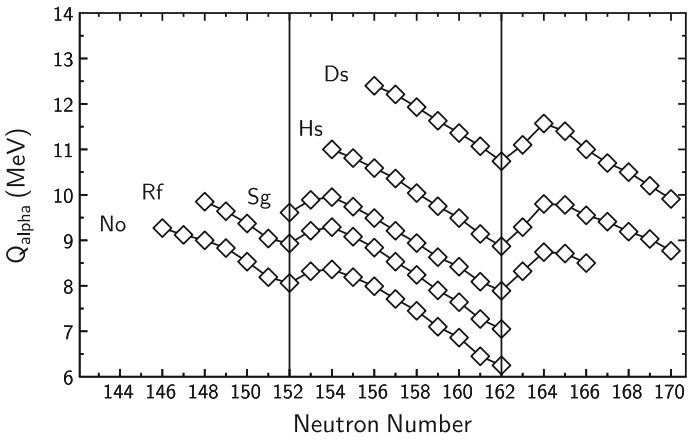

Fig. 19 Q-values calculated with the macroscopic-microscopic model versus neutron number. Data taken from [36, 37]

symmetry axis Ω. Thus, in deformed nuclei the level density appears to be much higher to begin with. However, each level now holds at most two nucleons and any gap in a Nilsson diagram directly leads to a low level density and therefore added stability.

In the region above $Z \simeq 100$ such gaps appear for neutron numbers 152 and 162 as well as proton number 108 (Hs). One consequence of this deformed gap is the occurrance of a local minimum in the alpha decay Q-value at 152 and 162 with local maxima at $N = 154$ and 164 respectively. In Fig. 19 we plot theoretical Q-values from [36, 37] in the region. The dips at $N = 152$ and 162 are clearly visible.

One would therefore expect the nucleus ^{270}Hs to exhibit all the characteristics of a nucleus with extra shell stabilization. This nucleus has recently been synthesized [38, 39] and its decay properties are indeed similar to those predicted.

Other indications of the deformed gap at $N = 152$ come from isomer spectroscopy. In a series of experiments the lowest excited isomeric states in ^{252,254}No and ^{250}Fm were investigated. The $N = 150$ isotones were assigned a neutron configuration while in the $N = 152$ isotope ^{254}No a proton character was established [22, 40]. This is entirely in line with the expectations from theory and supports the conclusions drawn from Q-values alone. Figure 20 shows the energies of the single particle states that play an important role around ^{250}Fm. Note that both protons and neutrons find pairs of levels close to the fermi level that can couple to low-lying states with high K, such as $(9/2^-[734]_\nu \otimes 7/2^+[624]\nu)^{8^-}$ for neutrons, or $(9/2^+[624]_\pi \otimes 7/2^-[514]_\pi)^{8^-}$ and $(7/2^-[514]_\pi \otimes 7/2^+[633]_\pi)^{6^-}$ for proton pairs. In systems with neutron number $N = 158$ one might reasonably expect high K configurations such as $(11/2^-[725]_\nu \otimes 7/2^+[613]_\nu)^{9^-}$ to form low lying isomeric states.

5 Experimental Techniques

The recent progress in nuclear spectroscopy techniques coupled with ever increasing sensitivities has allowed the full arsenal of in-beam nuclear spectroscopy techniques to be unleashed on heavier and heavier systems, produced with ever smaller cross sections. At the time of writing nuclei produced with cross sections as small as a few tens of nb can be studied.

These in-beam techniques are well established as sensitive tools in their own right and, when used for structure studies in superheavy nuclei, are generally complementary to decay studies following alpha or beta decay. In this section we will first look at the experimental conditions for in-beam gamma and electron spectroscopy, before discussing alpha spectroscopy and gamma spectroscopy after alpha decay.

5.1 Experimental Facilities

Experimental setups to study superheavy elements consist primarily of a recoil separator together with detector assemblies at the focal plane for discovery and decay experiments as well as surrounding the target position in case of in-beam studies. Detailed descriptions of each setup currently used in the world are available in the literature. Here we will focus on one example for a setup to explain the roles of the various detector systems in detail before summarising the properties of other widely used setups in a table.

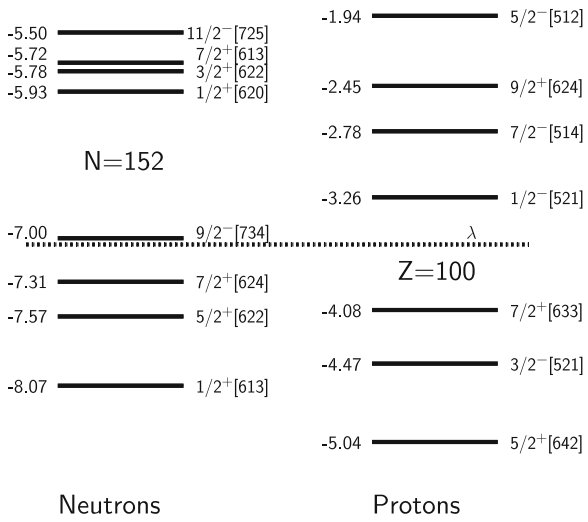

Fig. 20 Single particle energies for ^{250}Fm calculated using a Woods-Saxon potential with "universal" parametrization. The Fermi level is indicated by a *dashed line*. Adapted from [27]

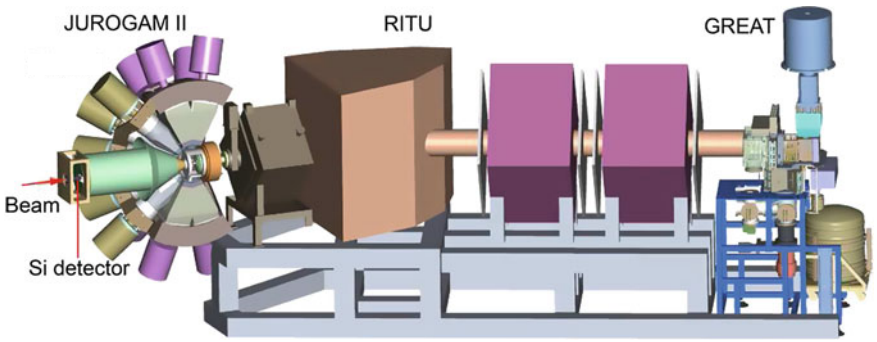

Fig. 21 Experimental in-beam spectroscopy setup at the Accelerator Laboratory of the University of Jyväskylä in Finland. The SAGE spectrometer [43] consisting of a Si detector and a solenoidal magnetic field together with the Jurogam II germanium detector array is on the *left* in front of the recoil separator RITU [44]. The focal plane of RITU is instrumented with the GREAT spectrometer [45]

Figure 21 shows a typical setup at the University of Jyväskylä, Finland. The centrepiece is formed by the gas-filled separator RITU [44], which has a transmission efficiency of approximately 40% for heavy evaporation residues while suppressing the primary beam and unwanted reaction products, e.g., from transfer reactions by more than eight orders of magnitude. The focal plane of RITU is equipped with the GREAT focal plane spectrometer [45]. Reaction products are implanted in two double-sided silicon strip detectors (DSSD) giving a total of 4800 pixels. In front of the implantation detectors sits a Multiwire Proportional Counter (MWPC) to measure the time of flight between the MWPC and the DSSD as well as the energy loss of the incoming ions and several PIN diodes forming a box in the forward direction to measure escaping alpha particles.

These elements are the minimum requirement for superheavy element research: a separator and a means to identify the reaction products. Alternatively a gas catcher is commonly used as a first stage for the transport to specialist detectors for chemical studies or transport to a trap. More details on gas-jet transport systems are given in "Synthesis of Superheavy Elements" and "Experimental Techniques".

For spectroscopy following decay this setup is extended by a variety of germanium detectors surrounding the implantation detector. In the GREAT spectrometer a segmented planar Ge detector is mounted in close proximity behind the DSSD to measure the X-rays and low energy gamma rays emitted at the focal plane. The whole setup is surrounded by several Clover detectors to measure the gamma rays emitted in the focal plane.

For in-beam studies the prompt radiation given off at the target position in front of the recoil separator has to be measured. In our example the detection of both gamma rays and conversion electrons is possible through the combination of the JUROGAM II array with a silicon detector forming the Silicon and GErmanium (SAGE) array. The JUROGAM II germanium array consists of 24 Clover detectors and 30 large single-crystal detectors with a total efficiency of 5.2% at 1.3 MeV.

Table 2 Experimental setups with recoil separators used in laboratories around the world for the study of superheavy elements.

Location	Separator	Configuration	Focal plane instrumentation	In-beam spectroscopy
Darmstadt GSI	SHIP [46, 47]	QQQEDDDDEQQQD[1] vacuum velocity filter	Recoil ID Ge detectors SHIPTRAP [48]	No
	TASCA [49]	DQQ gas-filled separator	Recoil ID Ge detectors (TASISpec) [50] chemistry	No
Dubna FLNR	VASSILISSA [51, 52]	QQQEEEQQQD vacuum E/q separator	Recoil ID Ge detectors (GABRIELA) [53]	No
	DGFRS [54, 55]	DQQ gas-filled separator	Recoil ID chemistry	No
Berkeley LNL	BGS [56]	QGD gas-filled separator	Recoil ID Ge detectors chemistry	GRETINA [57] gamma detection
Argonne ANL	FMA [58]	QQEDEQQ vacuum, mass analyser	Recoil ID Ge detectors	GAMMASPHERE [59, 60] gamma detection
Wako RIKEN	GARIS [61, 62]	DQQD	Recoil ID chemistry	No
Jyväskylä	RITU [44]	QDQQ gas-filled separator	Recoil ID Ge detectors	JUROGAM II [63] gamma detection SAGE [43] gamma and elecron detection

[1] *Q* quadrupole magnet; *D* dipole magnet; *E* electric field; *G* gradient field dipole magnet

A large number of experimental setups exist around the world that are optimized for the study of superheavy elements. The detailled description of each of them could easily fill a full chapter in this book. We shall therefore restrict ourselves to just list them here and give references where the interested reader can find more details. The information is summarized in Table 2. A more detailled overview of the setups relevant for in-beam gamma spectroscopy can be found in [27].

5.2 In-Beam Spectroscopy

In-beam spectroscopy has been the main tool used to uncover the structure of nuclei in great detail. Sophisticated methods to experimentally determine spins, parities, and underlying single particle configurations have been developed over many years and have allowed the detailed investigation of large and complex level

schemes of most nuclei. However, it is not straightforward to unleash this arsenal of spectroscopic tools in order to gain insights into the structure of nuclei with $Z \geq 100$. The main reason is the low cross section of the channel of interest relative to the total reaction cross section. One of the most favourable cases is the reaction of ^{48}Ca on ^{208}Pb which leads in the two-neutron evaporation channel to the production of ^{254}No with a cross section of 2 μb. To pull this weak channel out of the total reaction cross section of a few hundred mb, one has to employ recoil separators in order to identify those reactions leading to the channel of interest. This is not a problem unique to superheavy element spectroscopy. Whenever an experimental handle on a weak channel is required one is faced with the same principal problems. Thus a typical in-beam spectroscopy setup consists of a prompt gamma spectrometer, usually made up out of a large number of Compton suppressed Germanium detectors, coupled to a recoil separator with a suitable focal plane that allows the detection of the recoils of interest. If the focal plane of the separator is further equipped with a detector that allows the identification of the recoils via their characteristic alpha decays, one can employ Recoil Decay Tagging to pull very weak channels out of the background on an event-by-event basis.

The recoil decay tagging (RDT) technique is explained in Fig. 22, top panel. At time 0 a nuclear reaction happens at the target position and the emitted gamma rays are recorded in the Ge-array. The heavy recoil of interest then enters the separator and is transported to its focal plane with a flight time of a few microseconds, where it is implanted in a position sensitive focal plane detector. After a further time, the implanted recoil decays depositing the characteristic alpha decay energy in the same pixel. It is now possible to first use the spatial correlation to identify the implanted nucleus and then to use the well-defined flight time to identify the gamma rays emitted by this nucleus. The three spectra shown in Fig. 23 are taken at various stages of the RDT procedure. In the top panel all gamma rays observed in the reaction of ^{36}Ar on ^{144}Sm leading to a compound nucleus ^{180}Hg are shown [64]. The reaction is dominated by fission and transfer. None of the fission fragments and transfer products reach the focal plane of the recoil separator. The main reaction channel reaching the focal plane is the 2p-2n evaporation channel leading to ^{176}Pt. In the middle panel of Fig. 23 the gamma rays associated with all recoiling nuclei reaching the focal plane are shown. The ground state band of ^{176}Pt dominates the gamma spectrum. The channel of interest in the experiment, however, is the 4n evaporation channel leading to ^{176}Hg. This channel has only a small fraction of the total cross section. If one now further demands that the implanted recoil is followed within 60 ms by the characteristic alpha decay of ^{176}Hg, one obtains the spectrum shown in the bottom panel. As the gamma rays can be identified on an event-by-event basis, this spectrum of ^{176}Hg is extremely clean.

The situation for in-beam spectroscopy of superheavy elements is somewhat different. In the reaction of ^{48}Ca on ^{208}Pb typically only a single channel is open, i.e. the 2n channel leading to ^{254}No. Here the RDT technique is not used to pull a weak gamma ray signal out of an overwhelming background, but to ensure that the

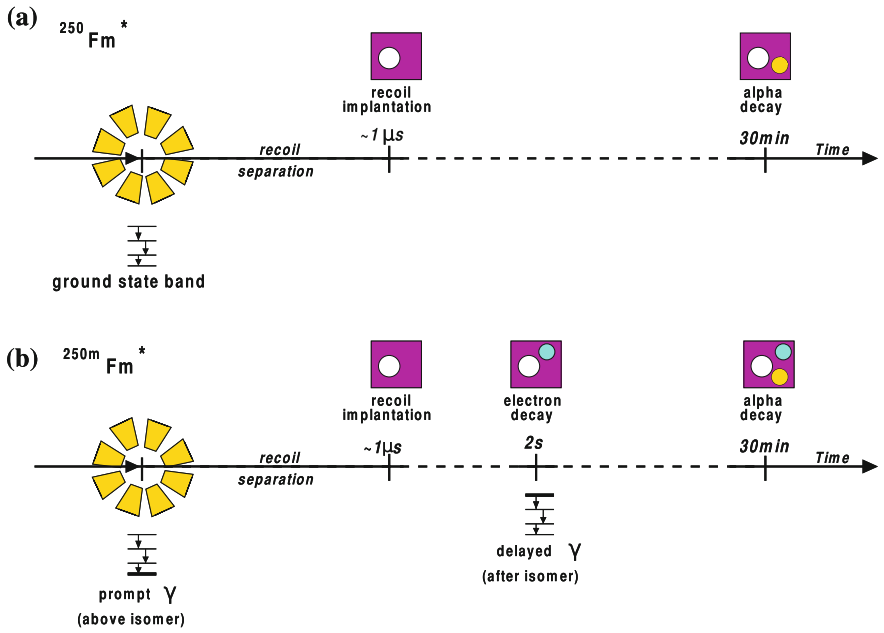

Fig. 22 Schematic illustration of the RDT technique. Prompt gamma rays are observed at the target position. The nucleus then recoils out of the target and flies through the separator where it is implanted in a Si detector. After a while the nucleus decays by a characteristic alpha decay in the same position, identifying the earlier implant. In the *bottom* panel a calorimetric electron signal additionally indicates the decay of an isomeric state

obtained spectrum is really associated with the nucleus in question. Figure 24 shows the gamma spectrum in coincidence with a recoil at the focal plane (top) and the gamma spectrum in coincidence with a recoil at the focal plane which has been correlated to a characteristic ^{254}No alpha decay taking place within 3 min after the implantation in the same pixel (bottom). The ground state rotational band is clearly visible. The intensity falls off for the lower spin members of the band as internal conversion begins to take over (see also Fig. 25). Thus the observed intensity maximum is at the $8^+ \rightarrow 6^+$ transition, and the $4^+ \rightarrow 2^+$ and $2^+ \rightarrow 0^+$ transitions can not be observed in gamma rays.

In the same way as the alpha tag one can use any decay signal at the focal plane to tag a particular reaction channel. The main application has been to tag on isomeric states in the recoiling nucleus. The principle shown in the bottom panel of Fig. 22 is as follows. If an isomeric state with a half-life longer than the flight time through the separator is populated in the reaction, then the isomeric state will decay after the nucleus has been implanted in the focal plane. When the isomer decays an energy signal is left in the implantation pixel from internal conversion electrons, low-energy X-rays, and Auger electrons. This signal is large enough to be detected and will eventually be followed by the ground state alpha decay. Thus

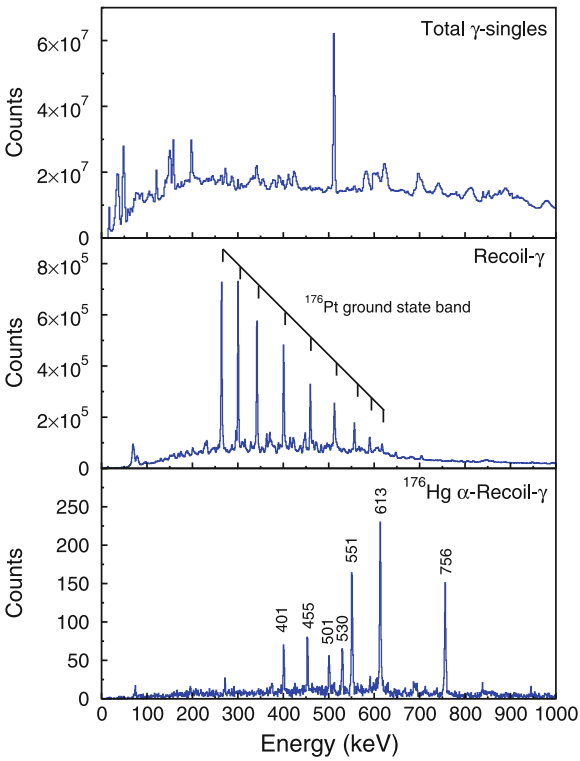

Fig. 23 Illustration of the RDT technique. The *top* panel shows all gamma rays emitted in the reaction of ^{36}Ar on ^{144}Sm. The *middle* panel shows all gamma rays associated with recoiling nuclei reaching the focal plane of the separator. The main reaction channel leading to ^{176}Pt is pulled out of the background. In the *bottom* panel only those gamma rays associated with implanted nuclei followed by the characteristic alpha decay of ^{176}Hg are shown [64]. Note the different scales on the axis. This technique is able to identify gamma rays belonging to a particular reaction channel on an event-by-event basis, which makes it so powerful

the characteristic sequence of implant, low-energy signal, and alpha decay can be used to identify isomers, and, analogous to the RDT technique, pull out the transitions populating the isomer from the prompt radiation measured at the target position. This process is illustrated in Fig. 26 for the decay of two isomeric states in ^{254}No [22]. The top two panels show the electron signals together with their time distributions. The short lived 184 μs isomer feeds mainly into the longer lived 266 ms isomer, and both gamma decay patterns are easily extracted through coincidence with the observed electrons (bottom panels).

5.3 Internal Conversion Electrons

In the heaviest nuclei transitions between excited states are dominated by internal conversion electron emission over gamma emission. It is important to realize that the emission of conversion electrons is a direct process, and does not proceed via an intermediate gamma ray. This is mainly due to the increased probability of finding an atomic electron (its wave function) inside the nucleus where energy can be transferred to it directly. We define the internal conversion coefficient α as the ratio of the number of electrons that get emitted to the number of gamma rays emitted during the decay of a sufficiently large ensemble:

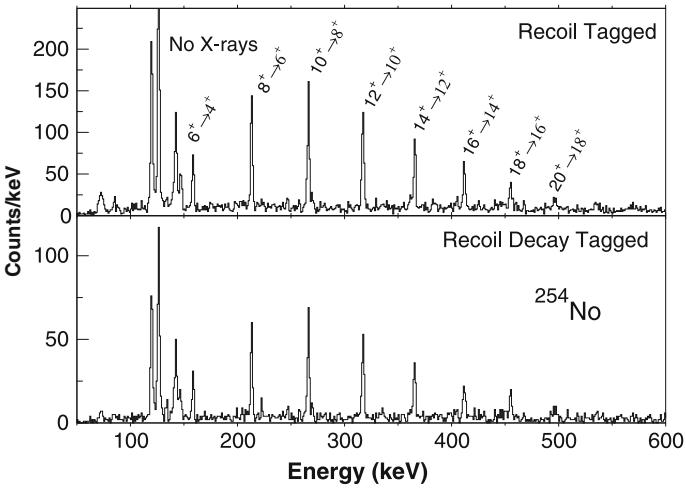

Fig. 24 Gamma ray spectra showing the ground state rotational band of ^{254}No. The *top* spectrum shows all gammas associated with recoils at the focal plane of RITU while the *bottom* spectrum shows only those gammas where the associated implanted nucleus was followed by a characteristic alpha decay of ^{254}No. All peaks in the top spectrum apart from the X-rays of Pb at 76–84 keV are confirmed to belong to ^{254}No

$$\alpha = \frac{I_e}{I_\gamma} \tag{27}$$

This means that a transition with a conversion coefficient of $\alpha = 1$ will proceed through equal numbers of gamma and electron decays if observed in a sufficiently large ensemble. Quantitatively the conversion coefficients increase with Z and increasing multipolarity as well as with decreasing transition energy. The total conversion coefficient is additively composed of the conversion coefficients for the different electron shells, i.e.

$$\alpha_{tot} = \alpha_K + \alpha_{L1} + \alpha_{L2} + \alpha_{L3} + \alpha_{M1} + \ldots \tag{28}$$

The coefficients are tabulated [65], but it is instructive to look at an approximate form valid for energies away from electron binging energy edges and transition energies not exceeding the electron rest energy by too much. Then the K conversion coefficient for an electric or magnetic transition with multipolarity L can be roughly approximated as [66]:

$$\begin{aligned} \alpha_K(EL) &\approx \frac{L}{L+1} Z^3 \left(\frac{e^2}{\hbar c}\right)^4 \left[\frac{2m_0c^2}{E_\gamma}\right]^{L+5/2} \\ \alpha_K(ML) &\approx Z^3 \left(\frac{e^2}{\hbar c}\right)^4 \left[\frac{2m_0c^2}{E_\gamma}\right]^{L+3/2} \end{aligned} \tag{29}$$

This form shows the general features:

- The conversion coefficient increases with decreasing transition energy. Note that as the energy drops below the binding energy of an atomic shell, the conversion coefficient changes rapidly near that threshold.
- The conversion coefficient increases with increasing multipolarity. Dipole transitions are less converted than quadrulole transitions.
- Magnetic transitions are more highly converted than electric transitions of the same multipolarity and energy.

For the spectroscopy of nuclei around $Z \simeq 100$ this means that $E2$ transitions below 200 keV as well as $M1$ transitions below 400 keV are dominated by internal conversion. A realistic case is calculated for fermium and shown in Fig. 25. Here the total conversion coefficients for $E2$ and $M1$ transitions are shown as a function of transition energy. We also show the coefficients for K-conversion in the same graph. It is clear that a measurement of the ratio of the K-conversion coefficient to the total conversion coefficient is sensitive to the multipolarity of the transition. Special attention has to be paid to transitions in the vicinity of binding edges where the conversion coefficient can vary rapidly with energy.

The 44 keV $2^+ \rightarrow 0^+$ transition in ^{254}No has a total conversion coefficient $\alpha \simeq 1500$ which makes this low-lying transition in the level scheme virtually undetectable in gamma rays. Conversely, if doing electron spectroscopy, this should be the strongest transition in the spectrum. Similarly, to deduce g-factors from branching ratios one needs the intensities of the stretched $E2$ transitions easily seen in gamma rays and the interband $M1$ transitions easily seen in electrons. The experimentalist therefore has to choose between gamma and electron spectroscopy, either of which will only reveal a partial picture of the level scheme. Efforts are underway to build a combined gamma and electron spectrometer (SAGE) at the University of Jyväskylä Finland, which will allow the simultaneous in-beam spectroscopy of heavy nuclei using gammas and conversion electrons [43].

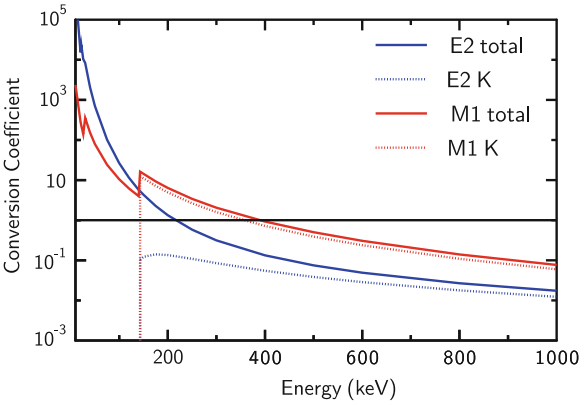

Fig. 25 Internal conversion coefficients for fermium calculated with BrICC [65]. The full lines show the total conversion coefficients for $E2$ and $M1$ transitions while the dashed curves show the K-conversion coefficients only

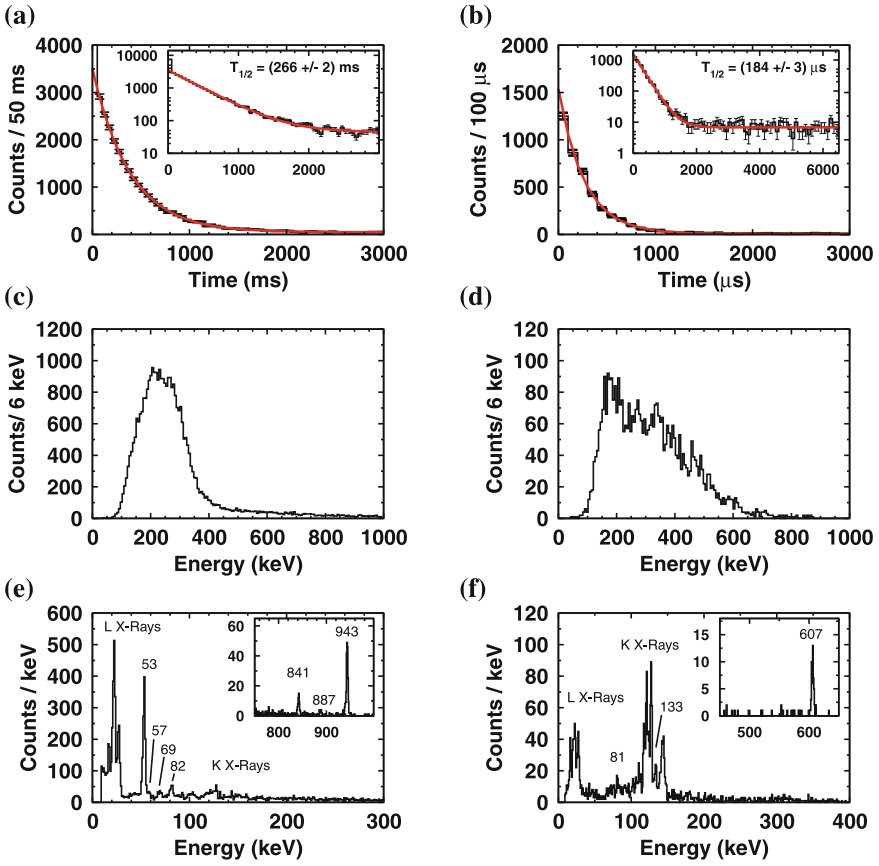

Fig. 26 Isomer spectra for ^{254}No. In panels **a** and **b** we show the time distribution between the implanted recoil and the observation of an electron signal. Note the different timescales for the two isomers. Panels **c** and **d** show the energy spectra of the observed electrons. The two decay paths of the isomers are clearly very different resulting in distinctly different electron signals. In panels **e** and **f** we show the associated gamma rays depopulating the isomers in coincidence with the electrons. The coincidence is able to clearly discriminate between the two different isomers

Selection rules for internal conversion largely follow the same rules as for gamma transitions, with one exception: $E0$ transitions between two states with angular momentum zero are forbidden for gamma rays, but allowed for internal conversion. This is due to the intrinsic angular momentum of the photon of 1 $\hbar$ which makes it impossible to fulfill the triangle rule. Electrons can, however, be ejected from the K shell with zero orbital angular momentum. The intrinsic spin of the electron does not enter the equation as the electron is not created in the process but acts as a spectator.

5.4 Decay Spectroscopy

Alpha decay can reveal a surprising amount of information about the decaying states. We shall not concern ourselves with the basic mechanisms of alpha decay but investigate how it can aid us in unraveling the nuclear single particle structure in the decaying system. The alpha decay half-life is determined by the probability to preform an alpha particle in the nucleus and the probability for that alpha particle to tunnel out of the nucleus. The former depends on the nuclear structure of the mother and the daughter states. The latter dominates the half-life so that we can use the concept of hindrance, i.e. the ratio of the probability that an alpha decay takes place relative to the probability of the same decay taking place in the absence of any influence of nuclear structure on the decay to get at the structural information.

In order to form an alpha particle one needs to assemble a pair of protons and a pair of neutrons. In even-even nuclei this is straightforward, and the most loosely bound pair of each type of particle has the highest probability of ending up in the alpha particle. In odd nuclei however one has a choice between breaking one pair and combining one of these nucleons with the previously single unpaired nucleon, or, alternatively, leaving the unpaired particle in place and forming the alpha particle from the first energetically available pairs. The situation is schematically indicated in Fig. 27. The former decay leaves the daughter nucleus in the ground state, while the latter decay prepares the daughter in an excited state with the odd particle occupying the same single particle orbital as it did in the ground state of the mother. We find experimentally that the latter process is greatly favored over the former. This means that by observing the most likely alpha decay in an odd mass decay chain we can deduce that the configuration and thus the spin and parity of the ground state of the mother and the excited state in the daughter are identical.

The great advantage of this method is that it allows us to trace single particle states from one nucleus to the next, and, since the identification of superheavy

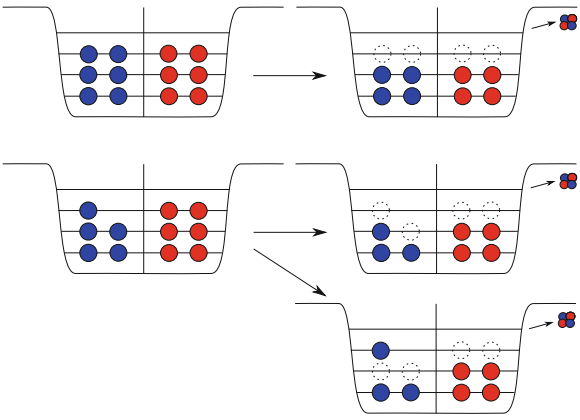

Fig. 27 Schematic illustration of the alpha decay. For an even-even nucleus the least bound pairs of nucleons are combined to form the alpha particle. In an odd–even nucleus the first pairs are usually used to form the alpha (*bottom*) leaving the daughter nucleus in an excited state, rather than breaking one pair (see text)

elements takes place mainly by observing its alpha decay chains, it tends to be readily available. The only observables required are the alpha decay Q-value and the observed half-life. Indeed, a large amount of data is available and the majority of our structural understanding of superheavy nuclei stems from alpha decay work (see, e.g., [27, 54, 67] for recent reviews). One drawback of the method is that it is usually not obvious where the populated state sits in the level scheme of the daughter nucleus, and thus it is difficult to relate the Q-value to the difference in the nuclear masses. In order to make full use of the information available one has to ensure that the radiation emitted during the decay to the ground state of the daughter nucleus is also measured.

5.4.1 Hindrance Factors

When studying alpha decays it is often advantageous to make use of the fact that the half-life of the decay is dominated by the barrier penetration, and that the influence of nuclear structure is of secondary importance. If one can separate the two components, then the influence of the nuclear structure on the decay can be readily studied. To this end one introduces the concept of hindrance. Here one compares the experimentally observed half-life $T_{1/2}^{exp}$ to a theoretical half-life $T_{1/2}^{theo}$ calculated under the assumption that the nuclear structure of mother and daughter have no influence on the decay whatsoever, see Eq. 30.

$$HF = \frac{T_{1/2}^{exp}}{T_{1/2}^{theo}} \tag{30}$$

Several different approaches to find a reasonable value for $T_{1/2}^{theo}$ can be found in the literature. One approach by Taagepera and Nurmia [68], valid for even-even nuclei, gives a semiempirical relationship between the half-life in years, the atomic number of the daughter Z and the alpha decay energy E_α in MeV (Eq. 31).

$$\log_{10} T_{1/2}^{\alpha} = 1.61(Z\sqrt{E_\alpha}) - Z^{2/3}) - 28.9 \tag{31}$$

Another frequently used approach goes back to Viola and Seaborg [69]. A more recent careful fit to a much larger available body of data has been given by Hatsukawa [70].

It is now straightforward to classify the observed alpha decays in terms of their hindrance factors. In even-even nuclei hindrance factors up to HF $\simeq$ 4 are commonly taken as unhindered or favoured transitions. The hindrance factor rises as the alpha decay comes with a change in angular momentum, and rises further still if the parity is changed during the transition. These statements are consciously left vague. While a direct comparison of two alpha lines connecting different states in the same mother-daughter system will give valueable clues about their relative angular momenta, the results of such a comparison should always be taken with a large grain of salt.

In odd mass nuclei hindrance factors rise sharply as the unpaired nucleon will have to either change the orbital it occupied or a pair has to be broken, as discussed in Sect. 5.4. The hindrance factors rise even higher in odd–odd nuclei, accounting for the need of both unpaired nucleons to either change orbital or the need to break one or two pairs.

5.4.2 Alpha Spectroscopy

Instead of implanting a recoiling heavy nucleus into a silicon detector it can be stopped in a gas volume. Transport from this gas-catcher to a gas chromatographic system then requires either a suitably volatile compound to be formed or transport via aerosols. Elements in groups 12–18 may even be transported directly in atomic form [71]. This introduces a chemical selectivity into the system which can be employed to greatly enhance the selectivity of the experiment. One big advantage of such a system is its continuous operation. Experimental details of such techniques are discussed in "Experimental Techniques" and results are outlined in "Gas-Phase Chemistry of Superheavy Elements".

As an example we turn to the chain of hassium isotopes. The state of the current understanding has been summarized recently by Türler [39]. Hassium readily forms the extremely volatile tetroxide HsO_4 which makes the chemical separation of Hs straightforward, provided the isotopes to be studied have a long enough half-life of at least the order of a milli-second. The method gives very clean alpha spectra typically unaffected by electron summing and the population of excited states in the daughters can be used to obtain a good idea of the level scheme of the daughters. In addition, the use of a thermochomatographic setup gave information on the volatility of the observed ^{269,270}Hs [72] which confirmed that hassium behaves similar to its lighter homologs in group 8 of the Periodic Table.

The isotopes ^{269}Hs, ^{265}Sg ^{261}Rf and ^{257}No are connected via alpha decays. However, the data obtained in a large number of experiments did not present an unabiguous picture. Recently, the available data has been reanalysed ([73] and references therein). Figure 28 shows the combined alpha spectra: The top panel shows all alpha decays attributed to ^{265}Sg. The next panel shows only those decays of ^{265}Sg where it was produced as an evaporation residue. This spectrum looks markedly different from that in panel c) where the alpha decays from ^{265}Sg produced in the alpha decay of ^{269}Hs are shown. This alone gives rise to the assumption that two alpha decaying states are present in ^{265}Sg. Further analysis of the daughter alphas show that the state in ^{261}Rf populated predominantly in the decays of ^{269}Hs in turn decays with a half-life of 3 s to ^{257}No. On the other hand, if ^{265}Sg is created as a fusion product, it predominantly decays to a state in ^{261}Rf which decays to ^{257}No with a half-life of 68 s.

On the basis of the combined dataset the following hypothesis was proposed [73]: Two alpha decaying levels in ^{265}Sg exist. Their half-lives are very similar, with 9 and 16 s, respectively. This similarity in half-lives makes a distinction on

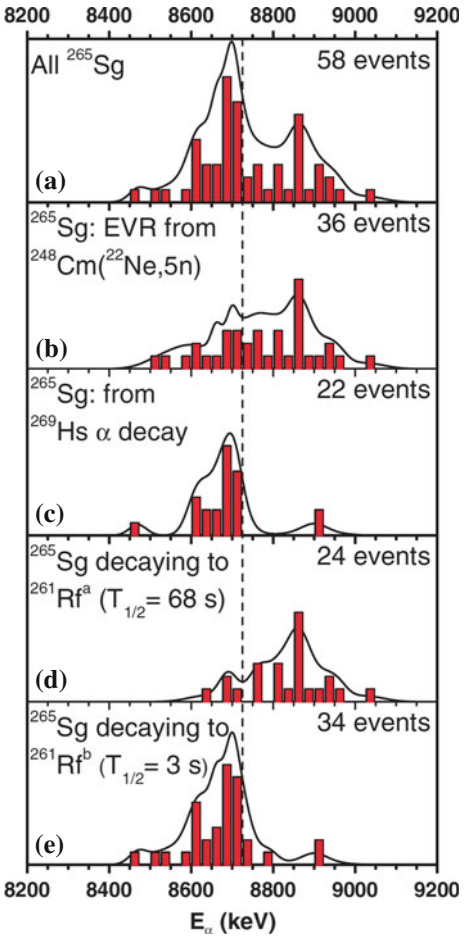

Fig. 28 Alpha spectra of events assigned to the decay of ^{265}Sg. *Solid lines* are superpositions of Gaussians taking into account the detector resolutions of the different detectors. Alpha decays are binned with a resolution of 25 keV. **a** All alpha decays of ^{265}Sg. **b** Only events of ^{265}Sg produced as an evaporation residue. **c** Only events where ^{265}Sg was the alpha decay product of ^{269}Hs. **a** is the sum of **b** and **c**. **d** Only events where ^{265}Sg populated the 68 s activity in ^{261}Rf. **e** Only events where ^{265}Sg populated the 3 s activity in ^{261}Rf. Reprinted figure with permission from [73]. Copyright (2008) by the American Physical Society

the basis of only a small number of events very difficult. These levels are populated to different degrees in the alpha decay of ^{269}Hs and a fusion evaporation reaction. Furthermore, both levels alpha decay to a pair of levels in ^{261}Rf with half-lives of 3 and 68 s, respectively, both of which populate ^{257}No. The proposed decay scheme is shown in Fig. 29. The conclusions of this analysis were recently fully confirmed (and refined) in an experiment performed at RIKEN [74]. This is a good example of the information that can be gathered through the observation of alpha energies and decay times alone.

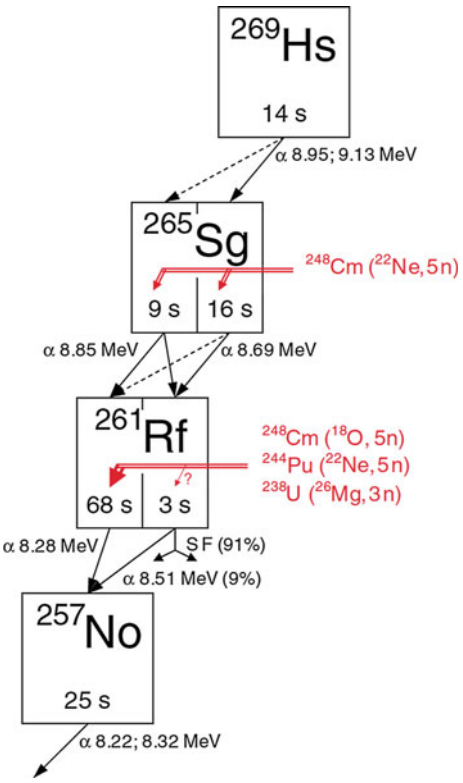

Fig. 29 Current working hypothesis of the decay pattern observed in the chain ^{269}Hs→ ^{265}Sg→ ^{261}Rf→ (^{257}No→). The dominant transitions are indicated with *solid lines*, weak transitions with *dashed lines*. Also shown is the approximate isomeric ratio when ^{265}Sg and ^{261}Rf are produced as evaporation residues. Reprinted figure with permission from [73]. Copyright (2008) by the American Physical Society

5.4.3 Spectroscopy Following Alpha Decay

Alpha decay gives as observables the energy of the decay, and, after kinematic correction the alpha decay Q-value, as well as the half-life. The quantity that is often required, however, is the mass of the decaying nucleus. In case of an even-even nucleus this is straightforward, as the unhindered main decay will connect the ground states of both nuclei and the Q-value directly gives the difference between the mass defects of mother and daughter.

This situation is greatly complicated in the odd–even and odd–odd cases. The presence of unpaired nucleons makes the assumption of a ground state to ground state transition invalid and the Q-value can only give a lower limit to the mass difference, as the alpha decay from the ground state of the mother can populate excited states in the daughter. The only way to obtain a nuclear mass from such a Q-value measurement is if one additionally has information about the excitation energy of the populated state in the daughter nucleus.

Such information is ideally obtained in the same experiment. If an alpha decay populates an excited state in the daughter nucleus, that state will decay to the ground state emitting radiation in prompt coincidence with the alpha particle. As

the probability for alpha decay depends exponentially on the Q-value the populated state will usually sit at fairly low energies in the daughter nucleus, usually well below 1 MeV. The populated state then decays via low energy transitions which are potentially highly converted, leading to the emission of one or more conversion electrons. If the decaying nucleus was implanted in a silicon detector, those electrons will be detected at the same time at the same place in the detector, thus producing an energy summing that can broaden an alpha peak considerably by spreading the alpha signal out to higher apparent energies. In order to obtain the cleanest alpha spectra one prefers to catch the activity on a surface and measure the emitted alpha particles in an external detector, thus greatly reducing the summing. This also leads to a reduction of the number of observed alpha particles due to the finite geometrical acceptance of such a setup.

Another way is to measure the gamma decays following alpha decay. As gamma rays are highly penetrating, they do not deposit a sizeable energy in a thin silicon detector and therefore do not contribute to a broadening of the alpha peak. They allow to build a level scheme for the daughter nucleus, thus fixing the energy of the populated state.

We shall illustrate this with an example. Figures 30 and 31 show the measured gamma ray spectra following the alpha decay of ^{253}No [75] and the systematics of the level schemes deduced from gamma spectroscopy following alpha decay in the $N = 151$ isotones. Three main gamma transitions are observed at 151, 222 and 280 keV in coincidence with the main alpha decay of ^{253}No, which are interpreted as transitions into the ground state rotational band of ^{249}Fm. Two further, much weaker transitions at 209 and 670 keV are in coincidence with alpha decays where the alpha has a different energy, and these are interpreted as hindered alpha decays to excited single particle configurations, which then decay to the ground state via the observed gamma transitions [75]. From this information the level scheme and the assigned configurations shown in Fig. 31 can be deduced.

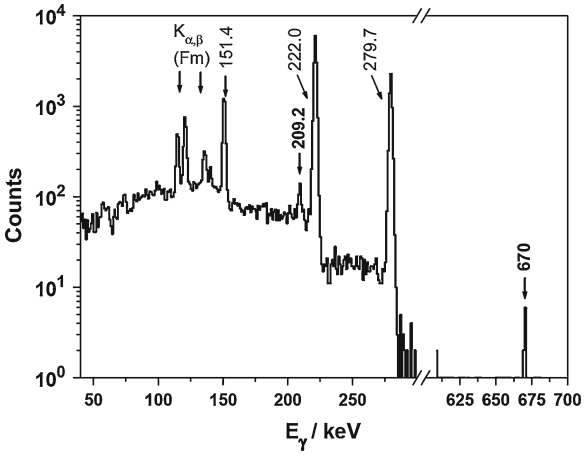

Fig. 30 Gamma rays observed following the alpha decay of ^{253}No. Figure reproduced from [75] with permission

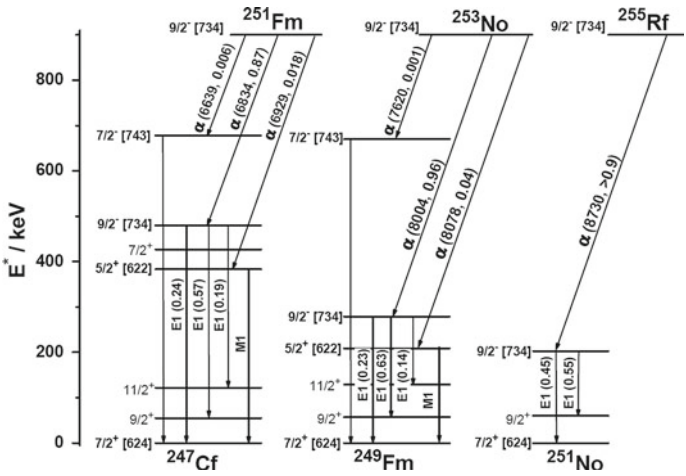

Fig. 31 Deduced level scheme compared to the neighboring $N = 151$ isotones. Taken from [75]

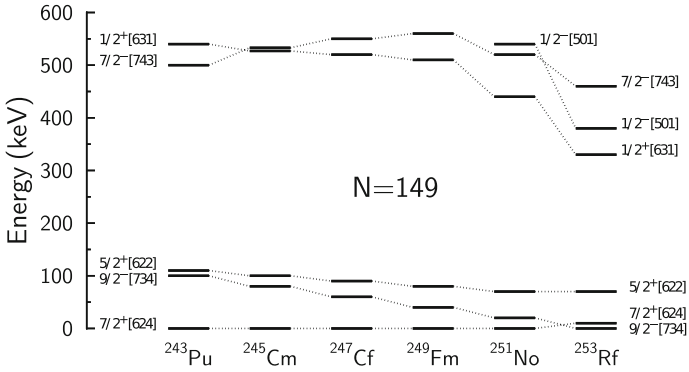

Fig. 32 Comparison of the calculated single neutron spectra for $N = 149$ isotones. The data is taken from [76], the figure is adapted from [27]

This level scheme should be compared to the calculated single particle spectra [76] shown in Fig. 32. The ground state in all cases is $7/2^+$. The lowering in energy of the $9/2^-$ state is nicely reproduced, while the $5/2^+$ and the higher lying $7/2^-$ configurations remain at roughly constant excitation energies.

The need for gamma spectroscopy after alpha decay at the focal plane of recoil separators has gained more and more importance over the last decade. This has lead to the development of a number of dedicated focal plane detection systems that place great emphasis on the detection of gamma rays. Examples include the GABRIELA setup in Dubna [53] and the GREAT spectrometer in Jyväskylä [45]. Currently the setup with the highest gamma ray detection efficiency is the TASISpec spectrometer [50] developed for the focal plane of the TASCA gas-filled separator at GSI [49].

In the TASISpec setup the geometry is optimized so that gamma rays from heavy nuclei implanted in the focal plane can be detected with an absolute efficiency of more than 50%. This paves the way for gamma spectroscopy on the heaviest systems where only a few nuclei are produced.

It is usually through a combination of experimental techniques that the structural assignments can be made. Direct measurements of nuclear masses can be an invaluable tool to determine the position of the level populated in alpha decay in the level scheme [77]. Ultimately, the problems accessing the superheavy region experimentally limits the number of possible experimental probes, and each nucleus has to be treated on an individual basis. This is one of the great experimental challenges for nuclear physics.

6 Conclusions and Outlook

The advances in nuclear experimental techniques over the last decades have allowed a step change in our understanding of the structure of the heaviest nuclei. The study of the rotational properties in in-beam experiments has shown up some of the best examples of rotational nuclei anywhere. Looking at isomeric states and the bands built upon them has allowed the assignment of single particle configurations to excited states which can then be used as a challenge to theory trying to reproduce and understand them. The use of conversion electron spectroscopy opens up a new approach to the study of the underlying single particle structure in the heaviest nuclei.

The rise of gamma spectroscopy after alpha decay has improved our understanding of the single particle configurations of and near the ground states of odd mass nuclei in a way that simply was not possible before. Many excited single particle configurations were identified through weak alpha decay branches and the detection of the subsequent gamma rays.

One obvious application of highly efficient gamma ray detection is in the identification of the elements produced. If an alpha decay populates an excited state in the daugther nucleus, it will decay and sometimes it will emit characteristic X-rays. If these X-rays can be detected, the identification of the Z of the daughter becomes straightforward. In a time when the identification of new elements via alpha decay chains ending in known elements increasingly fails to be applicable, this direct approach to the identification of the elements produced in a reaction will play an important role in the confirmation of claims of discovery.

The superheavy nuclei provide a unique testing ground for our understanding of the nuclus as a complex, strongly interacting many-body system. However, limitations in the number of nuclei that can be produced for study also restrict the number of probes that can be brought to bear. Often assignments are made on the basis of systematics, and need to be continuously confronted with newer measurements, and reevaluated as appropriate. Amongst the open questions is the role of isomers for the possibility of detecting superheavy elements in nature.

Identification of ground state configurations is crucial but experimentally difficult and not always possible on the basis of experimental data alone.

With the advent of modern radioactive beam facilities more neutron-rich systems will become available for study. Here the main challenge lies in the available beam currents, which are not yet high enough to reach a cross section in the picobarn region in a reasonable time. However, modern gamma arrays such as GRETINA and AGATA will be on hand to allow in-beam studies of some of the heaviest nuclei.

Chemical separation is an invaluable tool available for the longer-lived species, as they are chemically identified by the transport to a clean environment where low-backbround studies are possible.

Superheavy elements exist on the edge of physical possibility, both in terms of their electron configurations and their nuclear structure. They are difficult to produce and study, those we have studied so far do not exist long enough to allow any industrial application. Yet they open up a truly interdisciplinary field of study grounded in both chemistry and physics and they can teach us a great deal about the most extreme configurations of protons, neutrons and electrons available.

References

1. Goeppert-Mayer, M.: On closed shells in nuclei. Phys. Rev. **74**, 235–239 (1948)
2. Haxel, O., Jensen, J.H.D., Suess, H.D.: On the "Magic Numbers" in nuclear structure. Phys. Rev. **75**, 1766–1766 (1949)
3. Meldner, H.: Predictions of new magic regions and masses for super-heavy nuclei from calculations with realistic shell model single particle Hamiltonians. Ark. Fys. **36**, 593–598 (1967)
4. de Marcillac, P., Coron, N., Dambler, G., Leblanc, J., Moalic, J.-P.: Experimental detection of α-particles from the radioactive decay of natural bismuth. Nature **422**, 876–878 (2003)
5. Holden, N.E.: Total half-lives for selected nuclides. Pure Appl. Chem. **62**, 941–958 (1990)
6. Browne, E.: Nucl. Data Sheets **98**, 665–800 (2003)
7. Chukreev, F.E., Makarenko, V.E., Martin, M.J.: Nucl. Data Sheets **97**, 129–240 (2002)
8. Heyde, K.: Basic Ideas and Concepts in Nuclear Physics: An Introductory Approach, 3rd edn. Taylor & Francis, Bristol (2004)
9. Casten, R.F.: Nuclear Structure from a Simple Perspective. Oxford University Press, Oxford (2001)
10. Krane, K.S.: Introductory Nuclear Physics. Wiley, New York (1987)
11. von Weizsäcker, C.F.: Zur Theorie der Kernmassen. Z. Phys. **96**, 431–458 (1935)
12. Bethe, H.A., Bacher, R.F.: Nuclear physics A. Stationary states of nuclei. Rev. Mod. Phys. **8**, 82–229 (1936)
13. Wapstra, A.H., Gove, N.B.: The 1971 atomic mass evaluation. At. Data Nucl. Data Tables **9**, 267–468 (1971)
14. Huizenga, J.R., Vandenbosch, R.: Nuclear Fission. Academic Press Inc., New York (1974)
15. Armbruster, P.: On the production of heavy elements by cold fusion: The elements 106 to 109. Ann. Rev. Nucl. Part. Sci. **35**, 135–194 (1985)
16. Wagemans, T.C. (ed.): The Nuclear Fission Process. CRC Press, London (1991)
17. Schmidt, K.-H., Benlliure, J., Junghans, A.R.: Fission of nuclei far from stability. Nucl. Phys. A **693**, 169–189 (2001)

18. Halpern, I.: Nuclear fission. Annu. Rev. Nucl. Sci. **9**, 245–342 (1959)
19. Schädel, M.: The chemistry of superheavy elements. Act. Phys. Pol. B **34**, 1701–1728 (2003)
20. Blank, B., Chartier, M., Czajkowski, S., Giovinazzo, J., Pravikoff, M.S., Thomas, J.-C., de France, G., de Oliveira S.F., Lewitowicz, M., Borcea, C., Grzywacz, R., Janas, Z., Pfützner, M.: Discovery of doubly magic ^{48}Ni. Phys. Rev. Lett. **84**, 1116–1119 (2000)
21. Schneider, R., Friese, J., Reinhold, J., Zeitelhack, K., Faestermann, T., Gernhäuser, R., Gilg, H., Heine, F., Homolka, J., Kienle, P., Körner, H.J., Geissel, H., Münzenberg, G., Sümmerer, K.: Production and identification of ^{100}Sn. Z. Phys. A **348**, 241–242 (1994)
22. Herzberg, R.-D., Greenlees, P.T., Butler, P.A., Jones, G.D., Venhart, M., Darby, I.G., Eeckhaudt, S., Eskola, K., Grahn, T., Gray-Jones, C., Hessberger, F.P., Jones, P., Julin, R., Juutinen, S., Ketelhut, S., Korten, W., Leino, M., Leppänen, A.-P., Moon, S., Nyman, M., Page, R.D., Pakarinen, J., Pritchard, A., Rahkila, P., Saren, J., Scholey, C., Steer, A., Sun, Y., Theisen, Ch., Uusitalo, J.: Nuclear isomers in superheavy elements as stepping stones towards the island of stability. Nature **442**, 896–899 (2006)
23. Bender, M., Nazarewicz, W., Reinhard, P.-G.: Shell stabilization of super- and hyper-heavy nuclei without magic gaps. Phys. Lett. B **515**, 42–48 (2001)
24. Rutz, K. Bender, M., T. Bürvenich, T., Schilling, T., Reinhard, P.-G., Maruhn, J.A., W. Greiner, W.: Superheavy nuclei in self-consistent nuclear calculations. Phys. Rev. C 56, 238–243 (1997).
25. Bender, M. Rutz, K. Reinhard, P.-G., Maruhn, J.A., Greiner, W.: Shell structure of superheavy nuclei in self-consistent mean-field models. Phys. Rev. C 60, 034304(20) (1999).
26. Nilsson, S.G.: Binding states of individual nucleons in strongly deformed nuclei. Dan. Mat. Fys. Medd. **29**, 1–69 (1955)
27. Herzberg, R.-D., Greenlees, P.T.: In-beam and decay spectroscopy of transfermium nuclei. Prog. Part. Nucl. Phys. **61**, 674–720 (2008)
28. Worden, E.F., Gutmacher, R.G., Lougheed, R.W., Conway, J.G., Mehlhorn, R.J.: Hyperfine structure in the 253Es emission spectrum, II. Nuclear spin, nuclear magnetic dipole moment, and energy levels of Es II. J. Opt. Soc. Am. **60**, 1297–1302 (1970).
29. Baktash, C., Nazarewicz, W., Wyss, R.: On the question of spin fitting and quantized alignment in rotational bands. Nucl. Phys. A **555**, 375–407 (1993)
30. Bohr, A., Mottelson, B.R.: Nuclear Structure. World Scientific Publishing Co. Pte. Ltd, Singapore (1998)
31. Harris, S.M.: Higher order corrections to the cranking model. Phys. Rev. **138**, 509–513 (1965)
32. Herzberg, R.D., Amzal, N., Becker, F., Butler, P.A., Chewter, A.J.C., Cocks, J.F.C., Dorvaux, O., Eskola, K., Gerl, J., Greenlees, P.T., Hammond, N.J., Hauschild, K., Helariutta, K., Hessberger, F., Houry, M., Jones, G.D., Jones, P.M., Julin, R., Juutinen, S., Kankaanpaa, H., Kettunen, H., Khoo, T.L., Korten, W., Kuusiniemi, P., Le Coz, Y., Leino, M., Lister, C.J., Lucas, R., Muikku, M., Nieminen, P., Page, R.D., Rahkila, P., Reiter, P., Schlegel, C., Scholey, C., Stezowski, O., Theisen, C., Trzaska, W.H., Uusitalo, J., Wollersheim, H.J. : Spectroscopy of transfermium nuclei: $^{252}_{102}$No. Phys. Rev. C **65**, 014303(7) (2001).
33. Herzberg, R.D., Amzal, N., Bastin, J.E., Becker, F., Brew, P.M.T., Butler, P.A., Chewter, A.J.C., Cocks, J.F.C., Dorvaux, O., Eskola, K., Gerl, J., Greenlees, P.T., Hammond, N.J., Hauschild, K., Helariutta, K., Hessberger, F., Houry, M., Hurstel, A., Humphreys, R.D., Jones, G.D., Jones, P.M., Julin, R., Juutinen, S., Kankaanpaa, H., Kettunen, H., Khoo, T.L., Korten, W., Kuusiniemi, P., Le Coz, Y., Leino, M., Leppanen, A.P., Lister, C.J., Lucas, R., Muikku, M., Nieminen, P., Page, R.D., Page, T., Rahkila, P., Reiter, P., Schlegel, C., Scholey, C., Sletten, G., Stezowski, O., Theisen, C., Trzaska, W.H., Uusitalo, J., Wollersheim, H.J.: In-beam spectroscopy of ^{253,254}No. Eur. Phys. J. A **15**, 205–208 (2002)
34. Herzberg, R.D., Moon, S., Eeckhaudt, S., Greenlees, P.T., Butler, P.A., Page, T., Afanasjev, A.V., Amzal, N., Bastin, J.E., Becker, F., Bender, M., Bruyneel, B., Cocks, J.F.C., Darby, I.G., Dorvaux, O., Eskola, K., Gerl, J., Grahn, T., Gray-Jones, C., Hammond, N.J., Hauschild, K., Heenen, P.H., Helariutta, K., Herzberg, A., Hessberger, F., Houry, M., Hurstel, A.,

Humphreys, R.D., Jones, G.D., Jones, P.M., Julin, R., Juutinen, S., Kankaanpaa, H., Kettunen, H., Khoo, T.L., Korten, W., Kuusiniemi, P., LeCoz, Y., Leino, M., Leppanen, A.P., Lister, C.J., Lucas, R., Muikku, M., Nieminen, P., Nyman, M., Page, R.D., Pakarinen, J., Pritchard, A., Rahkila, P., Reiter, P., Sandzelius, M., Saren, J., Schlegel, C., Scholey, C., Theisen, C., Trzaska, W.H., Uusitalo, J., Wiens, A., Wollersheim, H.J.: Structure of rotational bands in ^{253}No. Eur. Phys. J. A **42**, 333–337 (2009)

35. Herzberg, R.-D., Cox, D.M.: Spectroscopy of actinide and transactinide nuclei. Radiochim. Acta **99**, 441–457 (2011)
36. Muntian, I., Hofmann, S., Patyk, Z., Sobiczewki, A.: Properties of heaviest nuclei. Acta Phys. Pol. B **34**, 2073–2082 (2003)
37. Muntian, I., Patyk, Z., Sobiczewski, A.: Calculated masses of heaviest nuclei (transl. from. Yad. Fiz). Phys. At Nucl. **66**, 1051–1055 (2003)
38. Dvorak, J., Brüchle, W., Chelnokov, M., Dressler, R., Düllmann, Ch.E., Eberhardt, K., Gorshkov, V., Jäger, E., Krücken, R., Kuznetsov, A., Nagame, Y., Nebel, F., Novackova, Z., Qin, Z., Schädel, M., Schausten, B., Schimpf, E., Semchenkov, A., Thörle, P., Türler, A., Wegrzecki, M., Wierczinski, B., Yakushev, A., Yeremin, A.: Doubly magic nucleus $^{270}_{108}\mathrm{Hs}_{162}$. Phys. Rev. Lett. **97**, 242501(4) (2006)
39. Türler, A.: Nuclear structure and reaction studies near doubly magic ^{270}Hs. Radiochim. Acta **100**, 75–83 (2012)
40. Greenlees, P.T., Herzberg, R.D., Ketelhut, S., Butler, P.A., Chowdhury, P., Grahn, T., Gray-Jones, C., Jones, G.D., Jones, P., Julin, R., Juutinen, S., Khoo, T.L., Leino, M., Moon, S., Nyman, M., Pakarinen, J., Rahkila, P., Rostron, D., Saren, J., Scholey, C., Sorri, J., Tandel, S.K., Uusitalo, J., Venhart, M.: High-K structure in ^{250}Fm and the deformed shell gap at $N = 152$ and $Z = 100$. Phys. Rev. C **78**, 021303(5) (2008)
41. Walker, P.M., Dracoulis, G.D.: Energy traps in atomic nuclei. Nature **399**, 35–40 (1999)
42. Hofmann, S., Hessberger, F.P., Ackermann, D., Antalic, S., Cagarda, P., Cwiok, S., Kindler, B., Kojouharova, J., Lommel, B., Mann, R., Münzenberg, G., Popeko, A.G., Saro, S., Schött, H.J., Yeremin, A.V.: The new isotope ^{270}110 and its decay products ^{266}Hs and ^{262}Sg. Eur. Phys. J. A **10**, 5–10 (2001)
43. Papadakis, P., Herzberg, R.D., Pakarinen, J., Butler, P.A., Coleman-Smith, P.J., Cresswell, J.R., Greenlees, P.T., Jones, P., Julin, R., Lazarus, I.H., Letts, S.C., Page, R.D., Parr, E., Peura, P., Pucknell, V.F.E., Rahkila, P., Seddon, D.A., Simpson, J., Sorri, J., Thornhill, J., Wells, D.: Towards combining in-beam gamma-ray and conversion electron spectroscopy. AIP Conf. Proc. **1090**, 14–20 (2009)
44. Leino, M., Äystö, J., Enqvist, T., Heikkinen, P., Jokinen, A., Nurmia, M., Ostrowski, A., Trzaska, W.H., Uusitalo, J., Eskola, K., Armbruster, P., Ninov, V.: Gas-filled recoil separator for studies of heavy elements. Nucl. Instr. Method B **99**, 653–656 (1995)
45. Page, R.D., Andreyev, A.N., Appelbe, D.E., Butler, P.A., Freeman, S.J., Greenlees, P.T., Herzberg, R.-D., Jenkins, D.G., Jones, G.D., Jones, P., Joss, D.T., Julin, R., Kettunen, H., Leino, M., Rahkila, P., Regan, P.H., Simpson, J., Uusitalo, J., Vincent, S.M., Wadsworth, R.: The GREAT spectrometer. Nucl. Instrum. Method B **204**, 634–637 (2003)
46. Münzenberg, G., Faust, W., Hofmann, S., Armbruster, P., Güttner, K., Ewald, H.: The velocity filter SHIP, a separator of unslowed heavy ion fusion products. Nucl. Instrum. Method **161**, 65–82 (1979)
47. Münzenberg, G., Faust, W., Hessberger, F.P., Hofmann, S., Reisdorf, W., Schmidt, K.-H., Schneider, W.F.W., Schött, H., Armbruster, P., Güttner, K., Thuma, B., Ewald, H., Vermeulen, D.: The velocity filter SHIP, performance and survey of current experiments. Nucl. Instrum. Method **186**, 423–433 (1981)
48. Block, M., Ackermann, D., Blaum, K., Chaudhuri, A., Di, Z., Eliseev, S., Ferrer, R., Habs, D., Herfurth, F., Hessberger, F.P., Hofmann, S., Kluge, H.-J., Maero, G., Martin, A., Marx, G., Mazzocco, M., Mukherjee, M., Neumayr, J.B., Plaß, W.R., Quint, W., Rahaman, S., Rauth, C., Rodriguez, D., Scheidenberger, C., Schweikhard, L., Thirolf, P.G., Vorobjev, G.,

Weber, C.: Towards direct mass measurements of nobelium at SHIPTRAP. Eur. Phys. J. D **45**, 39–45 (2007)
49. Semchenkov, A., Brüchle, W., Jäger, E., Schimpf, E., Schädel, M., Mühle, C., Klos, F., Türler, A., Yakushev, A., Belov, A., Belyakova, T., Kaparkova, M., Kukhtin, V., Lamzin, E., Sytchevsky, S.: The TransActinide Separator and Chemistry Apparatus (TASCA) at GSI—optimization of ion-optical structures and magnet designs. Nucl. Instrum. Method B **266**, 4153–4161 (2008)
50. Andersson, L.L., Rudolph, D., Golubev, P., Herzberg, R.D., Hoischen, R., Merchan, E., Ackermann, D., Düllmann, C.E., Eberhardt, K., Even, J., Gerl, J., Hessberger, F.P., Jäger, E., Khuyagbaatar, J., Kojouharov, I., Kratz, J.V., Krier, J., Kurz, N., Prokopowicz, W., Schädel, M., Schaffner, H., Schausten, B., Schimpf, E., Semchenkov, A., Türler, A., Wollersheim, H.J., Yakushev, A., Thörle-Pospiech, P., Hartmann, W., Hübner, A., Lommel, B., Kindler, B., Steiner, J.: TASISpec-A highly efficient multi-coincidence spectrometer for nuclear structure investigations of the heaviest nuclei. Nucl. Instrum. Method A **622**, 164–170 (2010)
51. Yeremin, A.V., Andreyev, A.N., Bogdanov, D.D., Chepigin, V.I., Gorshkov, V.A., Ivanenko, A.I., Kabachenko, A.P., Rubinskaya, L.A., Smirnova, E.M., Stepantsov, S.V., Voronkov, E.N., Ter-Akopian, G.M.: The Vassilissa facility for electrostatic separation and study of complete fusion reaction products. Nucl. Instrum. Method A **274**, 528–532 (1989)
52. Yeremin, A.V., Bogdanov, D.D., Chepigin, V.I., Gorshkov, V.A., Kabachenko, A.P., Malyshev, O.N., Popeko, A.G., Sagaidak, R.N., Ter-Akopian, G.M.: The electrostatic separator VASSILISSA Performance and experimental results. Nucl. Instrum. Method B **126**, 329–333 (1989)
53. Popeko, A.G., Belozerov, A.V., Briancon, Ch., Chepigin, V.I., Dorvaux, O., Hauschild, K., Kabachenko, A.P., Korichi, A., Lopez-Martens, A., Malyshev, O.N., Oganessian, Yu.: Ts., Saro, S., Shutov, A.V., Svirikhin, A.I., Yeremin, A.V.: GABRIELA setup for nuclear spectroscopy of the transfermium element isotopes at the VASSILISSA separator. Phys. At. Nucl. **69**, 1183–1187 (2006)
54. Oganessian, Y.: Heaviest nuclei from ^{48}Ca-induced reactions. J. Phys. G. **34**, R165–R232 (2007)
55. Tsyganov, YuS: The Dubna gas-filled recoil separator: status and developments. J. Phys. G **25**, 937–940 (1999)
56. Ninov, V., Gregorich, K.E., McGrath, C.A.: The Berkeley gas-filled separator. AIP Conf. Proc. **455**, 704–707 (1998)
57. Lee, I.Y., Clark, R.M., Cromaz, M., Deleplanque, M.A., Descovich, M., Diamond, R.M., Fallon, P., Macchiavelli, A.O., Stephens, F.S., Ward, D.: GRETINA: A gamma ray energy tracking array. Nucl. Phys. A **746**, 255–259 (2004)
58. Davids, C.N., Larson, J.D.: The argonne fragment mass analyzer. Nucl. Instrum. Method **40/41**, 1224–1228 (1989)
59. Lee, I.-Y.: The Gammasphere. Prog. Part. Nucl. Phys. **28**, 473–485 (1992)
60. Janssens, R.V.F., Stephens, F.S.: New physics opportunities at Gammasphere. Nucl. Phys. News **6**, 9–17 (1996)
61. Miyatake, H., Nomura, T., Kawakami, H., Tanaka, J., Oyaizu, M., Morita, K., Shinozuka, T., Kudo, H., Sueki, K., Iwata, Y.: INS gas-filled recoil isotope separator. Nucl. Instrum. Method B **26**, 309–313 (1987)
62. Morita, K., Yoshida, A., Inamura, T.T., Koizumi, M., Nomura, T., Fujioka, M., Shinozuka, T., Miyatake, H., Sueki, K., Kudo, H., Nagai, Y., Toriyama, T., Yoshimura, K., Hatsukawa, Y.: RIKEN isotope separator on-line GARIS/IGISOL. Nucl. Instrum. Method B **70**, 220–225 (1992)
63. Greenlees, P.T., Andreyev, A.N., Bastin, J., Becker, F., Bouchez, E., Butler, P.A., Cocks, J.F.C., Le Coz, Y., Eskola, K., Gerl, J., Hauschild, K., Helariutta, K., Herzberg, R.D., Hessberger, F.P., Humphreys, R.D., Hürstel, A., Jenkins, D.G., Jones, G.D., Jones, P., Julin, R., Juutinen, S., Kankaanpää, H., Keenan, A., Kettunen, H., Khoo, T.L., Korten, W., Kuusiniemi, P., Leino, M., Leppanen, A.P., Muikku, M., Nieminen, P., Page, R.D., Page, T.,

Pakarinen, J., Rahkila, P., Reiter, P., Schlegel, C., Scholey, C., Theisen, C., Uusitalo, J., Van de Vel, K., Wadsworth, R., Wollersheim, H.J.: Heavy element spectroscopy at JYFL. AIP Conf. Proc. **764**, 237–242 (2004)
64. Muikku, M., Cocks, J.F.C., Helariutta, K., Jones, P., Julin, R., Juutinen, S., Kankaanpää, H., Kettunen, H., Kuusiniemi, P., Leino, M., Rahkila, P., Savelius, A., Trzaska, W.H., Uusitalo, J., Greenlees, P.T., Page, R.D.: Probing the shape of ^{176}Hg along the yrast line. Phys. Rev. C **58**, R3033–R3036 (1998)
65. Kibedi, T., Burrows, T.W., Trzhaskovskaya, M.B., Davidson, P.M., Nestor Jr, C.W.: Evaluation of theoretical conversion coefficients using Br Icc. Nucl. Instrum. Method A **589**, 202–229 (2008)
66. Musiol, G., Ranft, J., Reif, R., Seeliger, D.: Kern-und Elementarteilchenphysik. VCH Verlagsgesellschaft, Weinheim (1988)
67. Leino, M., Hessberger, F.P.: The nuclear structure of heavy-actinide and trans actinide nuclei. Ann. Rev. Nucl. Part. Sci. **54**, 175–215 (2004)
68. Taagepera, R., Nurmia, M.: Ann. Acad. Sci. Fenn. Ser. A Phys. **78**, 1–17 (1961)
69. Viola, V.E., Seaborg, G.T.: Nuclear systematics of the heavy elements I, energetics and masses. J. Inorg. Nucl. Chem. **28**, 741–761 (1966)
70. Hatsukawa, Y., et al.: Systematics of alpha decay half-lives. Phys. Rev. C **42**, 674–682 (1990)
71. Pitzer, K.S.: Are elements 112, 114, and 118 relatively inert gases? J. Chem. Phys. **63**, 1032–1033 (1975)
72. Düllmann, C.E., Brüchle, W., Dressler, R., Eberhardt, K., Eichler, B., Eichler, R., Gäggeler, H.W., Ginter, T.N., Glaus, F., Gregorich, K.E., Hoffman, D.C., Jäger, E., Jost, D.T., Kirbach, U.W., Lee, D.M., Nitsche, H., Patin, J.B., Pershina, V., Piguet, D., Qin, Z., Schädel, M., Schausten, B., Schimpf, E., Schött, H.-J., Soverna, S., Sudowe, R., Thörle, P., Timokhin, S.N., Trautmann, N., Türler, A., Vahle, A., Wirth, G., Yakushev, A.B., Zielinski, P.M.: Chemical investigation of hassium (element 108). Nature **418**, 859–862 (2002)
73. Düllmann C.E., Türler, A.: ^{248}Cm(^{22}Ne,xn)$^{270-x}$Sg reaction and the decay properties of ^{265}Sg reexamined. Phys. Rev. C **77**, 064320(10) (2008)
74. Haba, H., Kaji, D., Kudou, Y., Morimoto, K., Morita, K., Ozeki, K., Sakai, R., Sumita, T., Yoneda A., Kasamatsu, Y., Komori, Y., Shinohara, A., Kikunaga, H., Kudo, H., Nishio, K., Ooe, K., Sato, N., Tsukada, K.: Production of ^{265}Sg in the ^{248}Cm(^{22}Ne,5n)^{265}Sg reaction and decay properties of two isomeric states in ^{265}Sg. Phys. Rev. C **85**, 024611(11) (2012)
75. Hessberger, F.P.: GSI experiments on synthesis and nuclear structure investigations of the heaviest nuclei. Eur. Phys. J. D **45**, 33–37 (2007)
76. Parkhomenko, A., Sobiczewski, A.: Neutron one-quasiparticle states of heaviest nuclei. Act. Phys. Pol. B **36**, 3115–3137 (2005)
77. Block, M., Ackermann, D., Blaum, B., Droese, C., Dworschak, M., Eliseev, S., Fleckenstein, T., Haettner, E., Herfurth, F., Hessberger, F.P., Hofmann, S., Ketelaer, J., Ketter, J., Kluge, H.-J., Marx, G., Mazzocco, M., Novikov, YuN, Plass, W.R., Popeko, A., Rahaman, S., Rodriguez, D., Scheidenberger, C., Schweikhard, L., Thirolf, P.G., Vorobyev, G.K., Weber, C.: Direct mass measurements above uranium bridge the gap to the island of stability. Nature **463**, 785–788 (2010)

http://www.springer.com/978-3-642-37465-4

The Chemistry of Superheavy Elements

Schädel, M.; Shaughnessy, D. (Eds.)

2014, XIII, 521 p. 217 illus., 48 illus. in color., Hardcover
ISBN: 978-3-642-37465-4